Capacitive Micromachined Ultrasound Transducers for Martian Anemometry

Submitted By
Gardy Kevin Ligonde

IN PARTIAL FULFILLMENT OF THE REQUIREMENTS FOR THE DEGREE OF

BACHELOR OF SCIENCE IN MECHANICAL ENGINEERING

School of Engineering
Tufts University
Medford, Massachusetts

May 2016

Signature of Author:
Gardy Kevin Ligonde

Committee:
Associate Professor Robert White
Department of Mechanical Engineering
Tufts University

Committee:
Research Assistant Professor Gary Leisk
Department of Mechanical Engineering
Tufts University

Abstract

The overall goal of goal of this project is to study the wind speed on Mars using sonic anemometry. The particular focus of this thesis is the ultrasound transducers needed for the instrument. Micromachined ultrasound transducers fabricated at Tufts University have been shown to work in Earth's atmosphere. In this thesis work, an effort has been made to understand how these devices would perform if placed in a Martian environment. The thesis provides an analysis of the behavior of two sensors with different structural dimensions. A special emphasis is placed on how pressure influences their undamped natural frequency and their quality factor. The validity of the modeling that has previously been used to design these transducers is also discussed. Finally, new fabrication techniques that were used to build a new sensor with a thinner structural membrane are presented. The undamped natural frequency of the device with a thicker membrane remained unchanged regardless of the pressure in the system. This is an agreement with computational models. On the other hand, the other device showed that the undamped natural frequency and the environmental pressure shared a proportional relationship; its resonant frequency decreased from 204 kHz at 760 Torr to 116 kHz at 1 Torr. This is also predicted by the models. In both devices, the quality factor increased with decreasing pressure as expected. The modeling used to predict the behavior of the system is accurate above 50 Torr. However, the quality factor is lower than predicted below 50 Torr due to other damping mechanisms that become dominant at low pressures. On the fabrication side, critical point drying was shown to be an effective method to reduce stiction. Initial experiments performed on electroless nickel plating indicate that it is a potential candidate for replacing nickel electroplating in the future, and may lead to better uniformity, and easier fabrication.

Acknowledgements

First and foremost, I must express my gratitude towards my advisor, Prof. Robert White, for giving me such a great learning experience. His continuous support, guidance, and motivation helped me in all of the time and effort that I put towards writing this thesis. I had not anticipated to learn as much as I did about microelectromechanical systems, nor did I expect my growth to extend beyond the focus of my research topic. Through his mentorship I have become more confident in my abilities to be successful as I transition to graduate school. I could not have imagined working with another advisor to complete my undergraduate research project.

I also have to thank Daniela "DT" Torres for sticking with me through this journey that started since last summer. We had no idea what we were getting into but I appreciate the fact that we supported each other and kept each other motivated through the numerous hours that were spent in the cleanroom. As frustrating as it got at times to start a process over, I feel that those moments helped us build character and taught us the importance of being tenacious.

That said, I would also like to thank James Vlahakis for his contributions to this project. I appreciate the times that he took to help out, especially when we needed to use the evaporator at Harvard. I am most appreciative of the fact that he offered me the opportunity to become a student microfabrication technician. Through training other microfab users, I feel that I improved my microfabrication skills and became more confident in handling some of the processes related to this project. Along with that, I'd also like to thank Wang Hyung-Sung for taking the time to help out with some of the evaporation processes that also needed to get done at Harvard.

Finally, I am grateful for having family and friends that have been extremely supportive throughout my senior year as I went through this research experience.

Table of Contents

Table of Figures

Table of Tables

1 Introduction

The performance of an existing capacitive micromachined ultrasound transducer (cMUT) array technology, and updates to this technology in terms of design and fabrication process, is described. For varying structural parameters and environmental conditions, frequency response measurements are taken and compared to computational models. Ultimately, the work presented here would be used towards the development of a sonic anemometer for a Martian environment. This chapter discusses the motivation for this research project as well as the contributions made.

1.1 Motivation

Our group, in collaboration with planetary scientists at Cornell University, is interested in studying atmospheric conditions that occur on Mars. It has been argued that the safety and success of future Mars expeditions depends on a better understanding of the surface's wind. From a pure scientific perspective, aeolian processes must be analyzed to estimate the stability of materials (i.e. H_2O, CO_2 frost) at or near the planet's surface. Furthermore, they would provide some insight on the origin and growth of dust storms that occur on the planet [1].

Previous technology for this study used variations of hot-wire anemometry, which measures the amount of power required to maintain a probe at a constant temperature. An advantage is that this approach is a relatively simple mechanical structure; however, it has several drawbacks. Firstly, its response time is too slow to measure turbulent fluctuations, which makes it difficult to accurately characterize the structure of the boundary layer of the surface. Second, heating or cooling sources may influence the probe measurements, so absolute calibration is challenging. Finally, this technology draws a relatively large amount of power during operation. Some of these limitations can be overcome through sonic anemometry, which is the focus of this thesis.

cMUTs have previously been developed at Tufts University as part of a Doppler velocity measurement system. They were capable of measuring the velocity of a moving object with a resolution of 5 cm/s [3]. The transducers performed this task by measuring the Doppler shift between emitted and detected ultrasonic waves. Using the operating principles of this existing technology, it is possible to use it in this new application where it will be measuring the velocity

of the wind. In other words, the cMUTs would be modified so that they could be used as a sonic anemometer.

1.2 Contributions

This thesis has made contributions to the modeling and the fabrication of the cMUT. While there already exists literature on cMUT operation at atmosphere, for the first time the capability in low pressure conditions was explored. This was accomplished by altering the air density during operation. An analysis was performed to understand how the quality factor and the undamped natural frequency of the device changed at the ambient pressure experienced at the surface of Mars. In addition, the structural properties influence on the parameters of interest was investigated. In this instance, the main structural properties were the thicknesses of the sacrificial and structural layers of the sensor. This information was additionally useful in providing some insight on how accurately the lumped element model (LEM) of a single transducer can predict its behavior at low pressures. Further contributions were made in the fabrication process of the devices. For the first time the applicability of evaporation, critical point drying, and electroless nickel plating in the production of the Tufts cMUT were examined.

2 Background

This chapter discusses relevant subjects pertaining to the cMUT, more specifically ultrasound, sonic anemometry, the device's history, and its operating principles.

2.1 Ultrasound & Applications

Ultrasound waves are patterns of disturbance caused by the movement of energy traveling through a medium such as air or water. A property of those waves is that they occur at relatively high frequencies, well above 20 kHz, which make them inaudible to human ears. As the wave travels through the air, it changes the density and pressure of the mediun along its direction of motion. Figure 2-1 illustrates how particles are displaced due to pressure fluctuations caused by the vibration from a source.

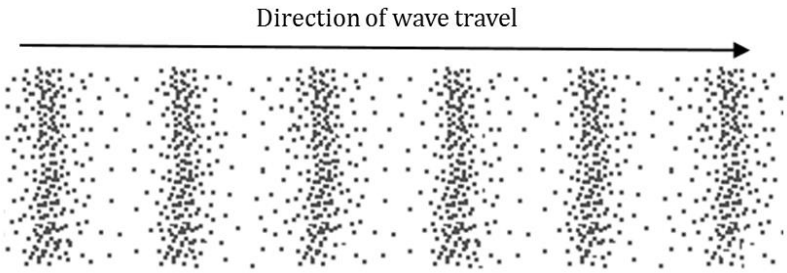

Figure 2-1 - Regions of high and low density caused by pressure fluctuations. Figure taken from http://www.mediacollege.com/audio/images/loudspeaker-waveform.gif

Ultrasonic devices are used in a variety of fields, usually to detect objects and measure distances. For instance, ultrasonography is a medical imaging technique that is used to visualize internal body structures such as tendons, muscles, joints, and organs. Using a probe, high-frequency signals are sent through a body. As they hit a boundary (i.e. between fluid and soft tissue) some signals get reflected back to the probe while others continue to travel until they reach another boundary. Using the material properties of the medium and the time of travel, machines are capable of calculating the distances traveled from the probe and can display them as two-dimensional images on a screen. Many ultrasonic commercial medical devices use piezoelectric or piezocomposite transducers; however, capacitive transducers have been considered as an alternative because of advantages they provide [4].

Ultrasound also plays a significant role in robotic and automatic applications, as it is useful for certain processes such as object identification, position tracking, and obstacle avoidance. One technique, known as the time-of-flight (TOF) mode, can be used to measure the distance between a transmitter and a target. This measurement is obtained by counting the time elapsed from the instant a short train of waves is emitted to the instant that it arrives in the receiver. Another technique, known as the continuous-wave method, measures the referred distance by detecting the phase shift between the transmitted and received signals. Whereas TOF duration limits the rate at which measurements can be made, the continuous wave method can provide the accuracy and speed required by many automatic utilities [5].

Another application of ultrasound signals takes place in underwater wireless communication. Since the absorption of electromagnetic energy in a conductive medium like seawater is extremely high, radio waves tend to fail; however the absorption of sound is about

three orders of magnitude lower. As a result, an underwater telephone has been developed for communicating with small submersibles engaged in archeological search [6-7].

2.2 Capacitive Micromachined Ultrasound Transducers

The following section briefly describes the history of the CMUTs, their operating principles, as well as their performance in a Martian environment.

2.2.1 History

Historically, piezoelectric crystals, ceramics, polymers and piezocomposite materials were generally used to generate and detect ultrasound signals. Although the idea of electrostatic or capacitive transducers was known for a while, it was not popularized due to the high electric fields that are required in order to achieve acceptable frequencies. Recent advances in microfabrication technology have made it possible to build capacitive transducers that are able to compete with piezoelectric transducers. During the 1980s and early 1990s, the first micromachined electrostatic transducers were reported. These devices were not well characterized and the fabrication process was not simple. It wasn't until 1993 that advanced IC fabrication processes enabled the realization of submicron gaps between electrodes that would make it possible to achieve high electric fields. The first cMUTs that incorporated these features were designed by M. Haller and B. T. Khuri-Yakub [8].

2.2.2 Physical principle

In order to generate and detect ultrasound signals, the cMUT consists of two electrodes separated a by a thin air gap. The top electrode, a very thin membrane, is equipped with relatively small holes to allow air to circulate between the environment and the cavity within the device. The pressure of an incoming wave causes the membrane to deflect toward the bottom electrode. The vent holes that allow air to flow into the backing cavity serve as a damping force, causing the system to lose energy. The stiffness of the membrane as well as the pressure within the cavity cause the membrane to deflect in the opposite direction. Since ultrasound waves consist of regions of high and low pressure, the membrane oscillates accordingly. Electrically, this

configuration, as seen in Figure 2-2, is a parallel plate capacitor. Thus, it is possible to determine the deflection of the diaphragm, and therefore the received ultrasound energy, based on the change in capacitance resulting from the oscillations of the top electrode.

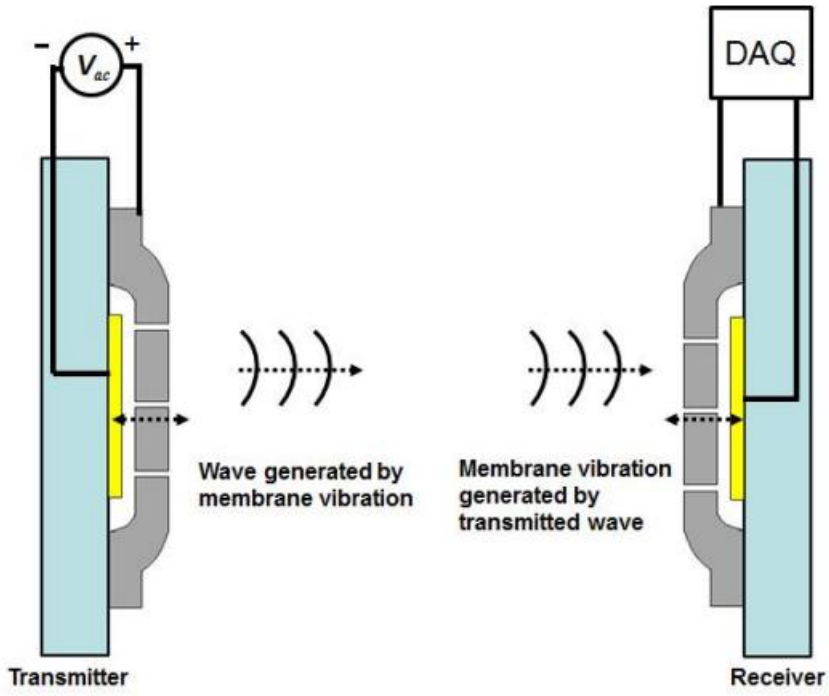

Figure 2-2 - Schematic of a cMUT. Figure taken from [3]

Similarly, if a voltage is applied between the electrodes, then an electrostatic force is induced, causing the membrane to deflect towards the substrate. However, once the voltage is removed, the stiffness of the membrane will cause it to oscillate. Meanwhile, the viscous effects from the air surrounding the membrane and flowing through the vent holes will cause the system to lose energy until it returns to its original position. By generating AC signals, it is possible to cause the membrane to transmit ultrasound waves through its high frequency oscillations.

2.2.3 Mars Application

The purpose of this project is to design cMUTs that can measure wind velocity in a Martian environment. A simple 3D sonic anemometer is built by arranging six cMUTs such that each

transmitter-receiver pair forms a vector perpendicular to the other two pairs. Such a configuration can be seen in Figure 2-3.

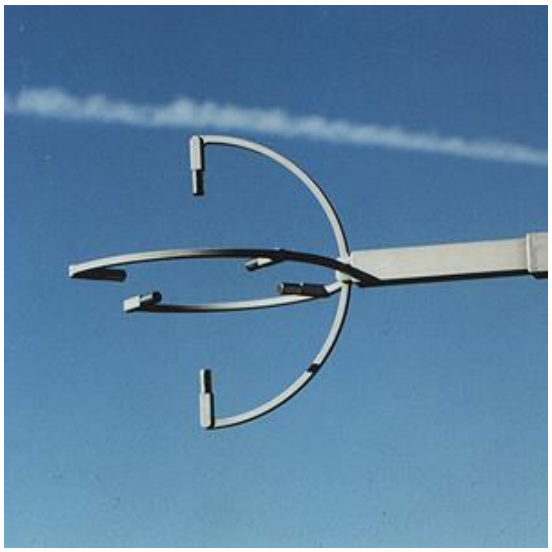

Figure 2-3 - Sonic anemometer. Figure taken from http://www.apptech.com/images/vxprobe.jpg

Since the distance between the sensors is known, the wind velocity can be determined based on the time of flight of a signal from a transmitter to a receiver. A simple illustration explaining this process can be seen in Figure 2-4.

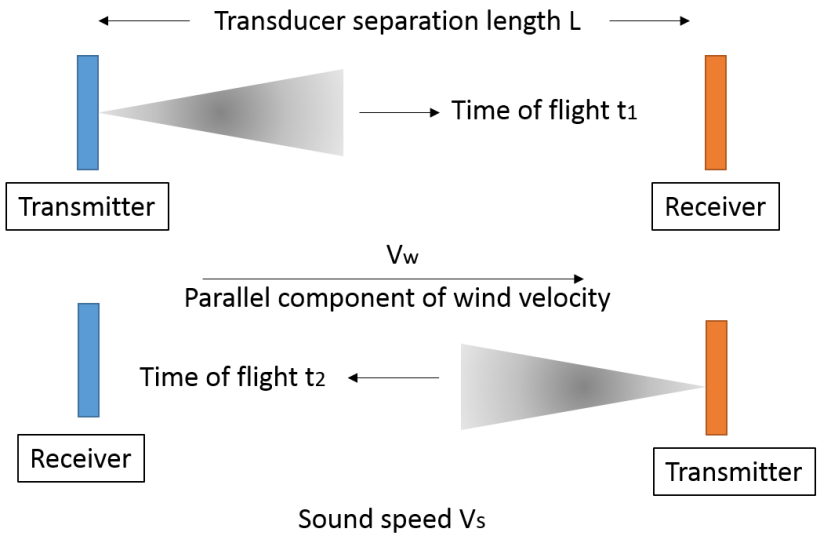

Figure 2-4 - Basic operating principle of sonic anemometer

$$v_w = \frac{L}{2}\left(\frac{1}{t_1} - \frac{1}{t_2}\right) \quad (1)$$

$$v_s = \frac{L}{2}\left(\frac{1}{t_1} + \frac{1}{t_2}\right) \quad (2)$$

First, the time of flight t_1 of a signal from a transmitter to a receiver is recorded. Then, the roles of the sensors are switched such that the receiver becomes the transmitter, and vice-versa. Finally, the time of flight t_2 of a signal from the new transmitter-receiver pair is recorded. With the known separation distance L, equations (1) and (2) can be used to determine the wind velocity and the sound speed.

2.2.4 Redesign and LEM

A plot that shows the expected performance of the cMUT in an environment composed of CO_2 at the pressure of the Martian surface (6 mbar) is seen in Figure 2-5. The narrow band output near the undamped natural frequency indicates that the damping ratio at 6 mbar is much smaller than atmosphere. In other words, it would be difficult to gather reliable measurements near that frequency since the transmit pressure would vary significantly with any slight changes in the frequency of the signal. Consequently, the device would have to operate off-peak. It is also known that attenuation of the signal would have a stronger influence at 6 mbar relative to atmospheric pressure as there would be less total energy present in the signal. In order to have a strong signal strength, one solution would involve decreasing the natural frequency of the cMUTs and reducing the sense gap height. Furthermore, operation at a lower frequency would reduce attenuation, as its effects decrease at low frequencies.

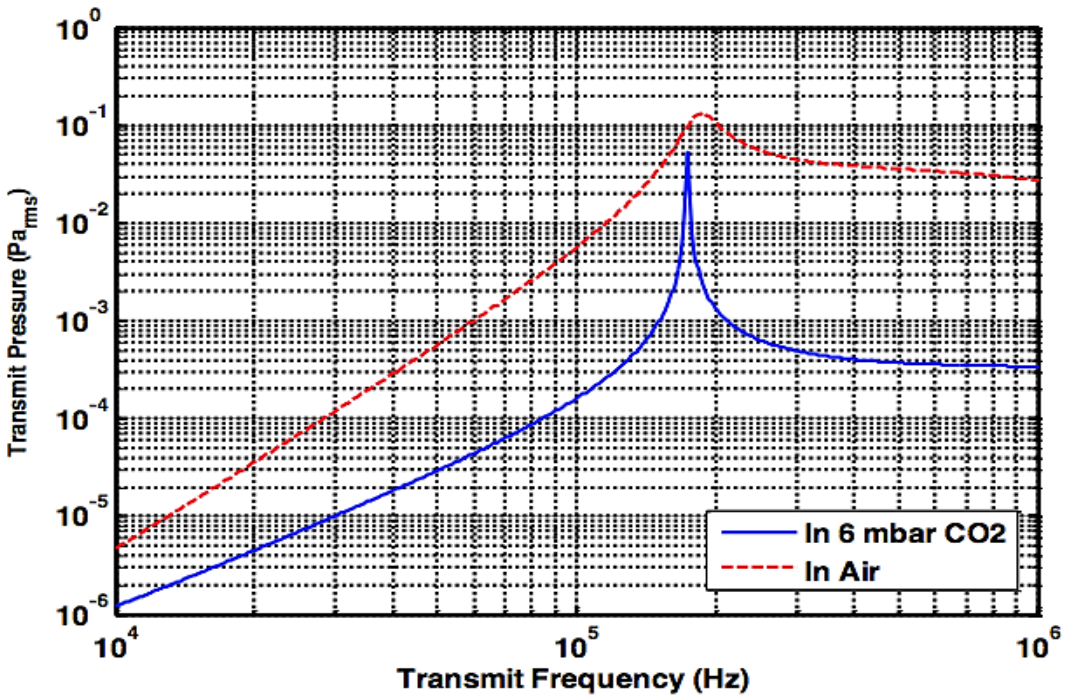

Figure 2-5 - Predicted response of the cMUT at atmospheric pressure and 6 mbar

In a journal paper on a *Micromachined ultrasonic Doppler velocity sensor using nickel on glass transducers*, Shin *et al* describe the lumped element modeling (LEM) of a single transducer [2]. The LEM includes the diaphragm mechanics, the backing cavity compliance, squeeze film damping, and environmental loading, as well as the mechanical-electrical coupling of the electrostratics. As seen in Figure 2-6, there are various elements in the system that can be represented two different ways.

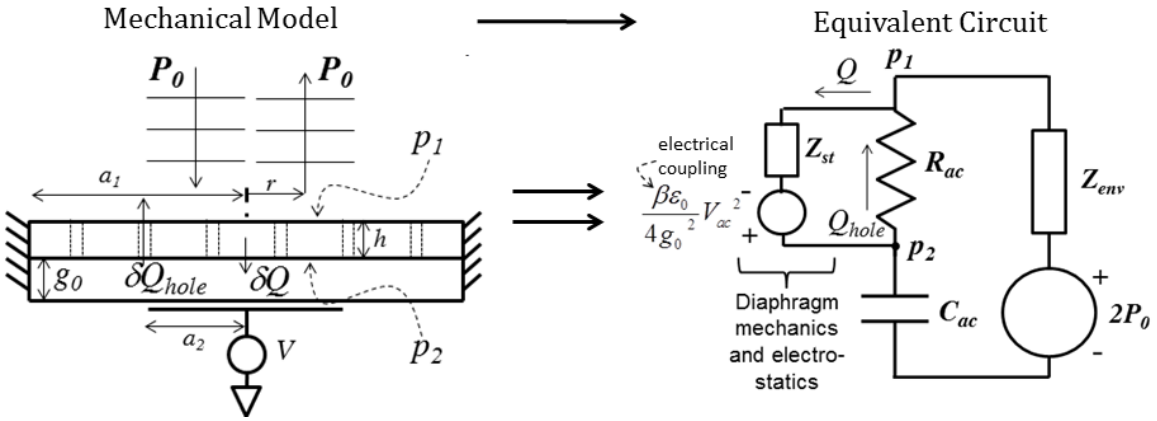

Figure 2-6 - Coupled mechanical-electrical lumped element model. Figure from an unpublished talk given by Prof. White at the "University of Vermont ME Seminar Series and Vermont Space Grant Consortium".

Through the methods described in the LEM, it is possible to determine the expected behavior of the system based on changes made to any of the parameters. An equation that is of particular interest for this research is the components that determine the undamped natural frequency of the system. As seen in equation (3), the three parameters of interest are the effective mass of the diaphragm (M_{dia}), its compliance (C_{dia}), as well the compliance of the backing cavity (C_{cav}). While both M_{dia} and C_{dia} are related to the thickness of the membrane, the compliance of the cavity is affected by the gap height and the density of the environment [2]. Consequently, there are two possible scenarios that may occur as the pressure during operation decreases:

1. The compliance of the air cavity is significant; the undamped natural frequency will depend on the pressure.
2. The compliance of the diaphragm is a dominant; the undamped frequency will not depend strongly on pressure.

$$\omega_n = \sqrt{\frac{1}{M_{dia}}\left(\frac{1}{C_{dia}} + \frac{1}{C_{cav}}\right)} \tag{3}$$

3 Design and Fabrication

In this chapter, the fabrication process of the cMUT is discussed. It is organized in three sections. First, the structure of the device is shown. Then, the new techniques that were incorporated as part of the thesis are presented. Finally, a section considers the possibility of incorporating electroless nickel plating in future fabrication processes is included.

3.1 Nickel-on-glass chip

This section describes the structure of the cMUT as well as the new fabrication methods that were used for the redesigned transducer.

3.1.1 Structure

The nickel-on-glass cMUT sensor consists of three components. First, there is a 600µm diameter membrane, which serves as the top electrode. Then, there is an anchor, and finally a 390µm diameter bottom electrode (Figure 3-1).

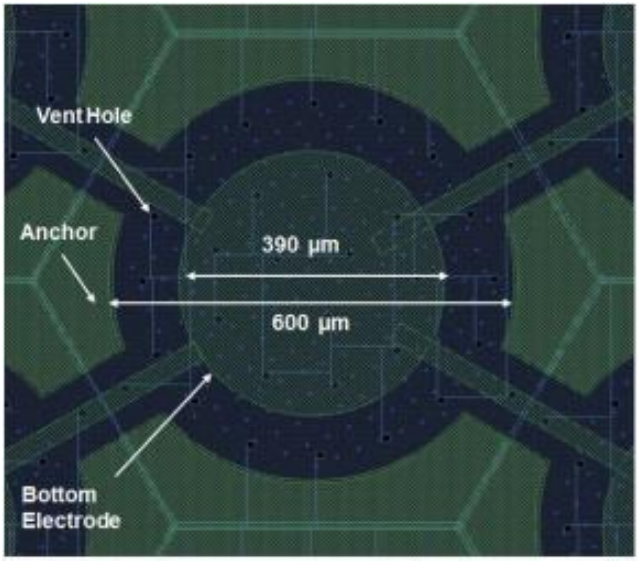

Figure 3-1 - Schematic of a single element (top view). Figure taken from [3].

3.1.2 Fabrication

The fabrication process can be described in eight major steps, illustrated in Figure 3-2. While each one is described below, a runsheet for the most recently fabricated cMUTs as of the completion of this thesis is shown in Appendix A. The cMUT sensor was fabricated at the Tufts Micro- and Nano- Fabrication facility (TMNF).

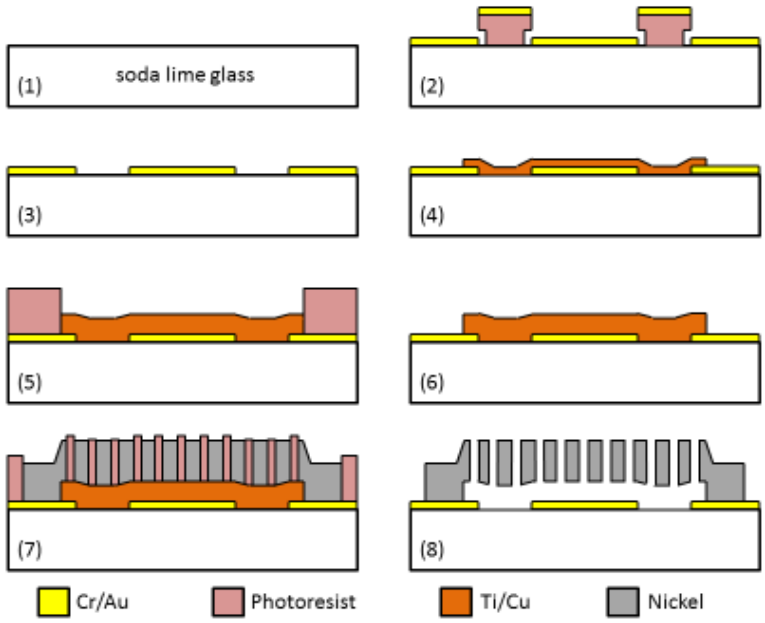

Figure 3-2 - Fabrication process involving copper and nickel electroplating

(1)

A 550 µm thick soda lime glass wafer is cleaned by submerging it in a piranha solution for 10 minutes to clean any organic residues that may be present. An oxygen plasma clean follows to ensure organic residues have been removed.

(2)

The bottom electrode is patterned on the wafer through a lithography step, which makes use of liftoff resist (LOR) and AZ 9260 photoresist. The two methods of building the bottom electrode are described:

Table 3-1 - Deposition methods for cMUT bottom electrode

Previous Method: Sputtering	**New Method: Evaporation**
Device: Nanomaster NSC-3000 DC Magnetron Sputter Tool Cr thickness: 10 nm Au thickness: 70 nm	Device: Edwards Auto 306 e-beam evaporator Cr thickness: 15 nm Au thickness: 150 nm

During the course of this research, it was observed that a residue remained on the bottom electrode after a cMUT process was finished (Figure 3-3). While none of the membranes collapsed, the devices were still defective. It was suggested that the residue might have played a role in causing the devices to be faulty. Consequently, all sputtering procedures in the previous runsheet were replaced by evaporation. The expectation was that higher quality films would be obtained.

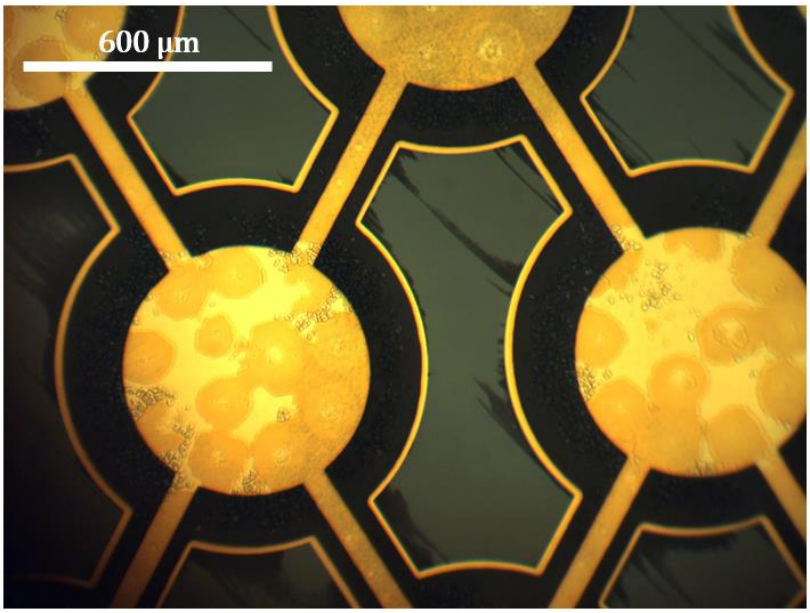

Figure 3-3 - Residue present on bottom electrode of cMUT

(3)

The photoresist is then removed by submerging the wafer in a solution of Remover 1165 for 3 hours. Then it is sonicated for 5 minutes to remove any particles that may still be present on the surface. The wafer now consists of its bottom electrode and bonding pads, as shown in Figure 3-4.

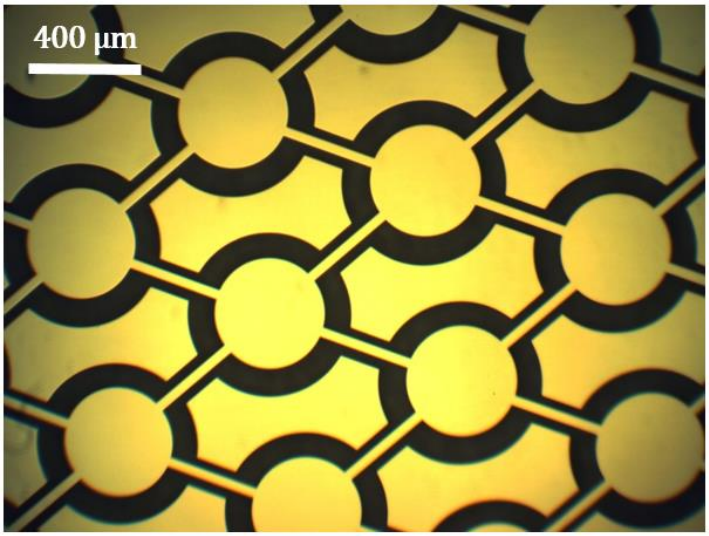

Figure 3-4 - Cr/Au bottom electrodes successfully patterned

(4)

Similarly to the second step, the sacrificial layer is patterned on the wafer using LOR and AZ 9260 photoresist. Then, the seed layer, which is composed of titanium and copper, is deposited. Then, a liftoff is performed along with a sonication to prepare the wafer for the next step, which involves building the sacrificial layer (Figure 3-5).

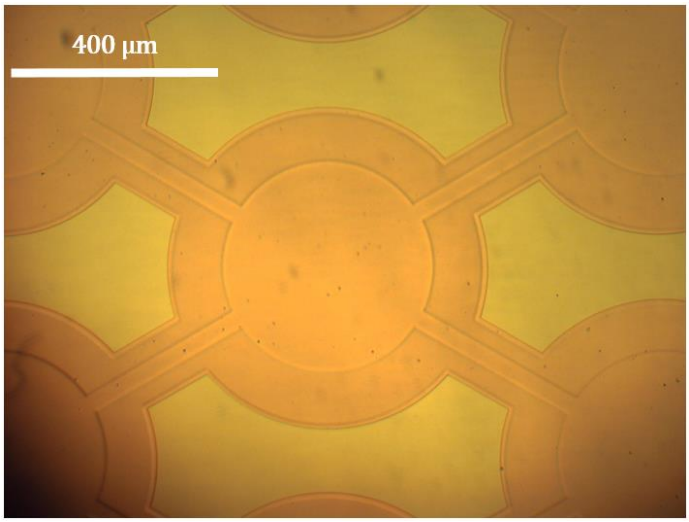

Figure 3-5 - Ti/Cu seed layer after liftoff

Table 3-2 - Deposition of Ti/Cu seed layer

Previous Method: Sputtering	New Method: Evaporation
Device: Nanomaster NSC-3000 DC Magnetron Sputter Tool Ti thickness: 30 nm Cu thickness: 300 nm	Device: Edwards Auto 306 e-beam evaporator Ti thickness: 30 nm Cu thickness: 300 nm

(5)

A lithography step is next performed using AZ 9260 with thicker photoresist (~8 µm). Then the sacrificial layer is deposited through copper electroplating. Two copper plating methods are shown below:

Table 3-3 - Copper electroplating parameters

Previous Method	New Method
"Technic Copper FB Bath Ready to Use" *Contains*: copper sulfate (5-10%), sulfuric acid (15-20%), chloride ions, and brightener Current density: 5mA/cm^2 Expected deposition rate: 100 nm/min	*"Homemade" solution with materials from Technic* *Contains*: 1.5 M sulfuric Acid, 0.8 M Copper sulfate, 80 ppm Cl^- ions Current density: 13mA/cm^2 Expected deposition rate: 320 nm/min

(6)

The photoresist is stripped by soaking the wafer in acetone, isopropanol, and water.

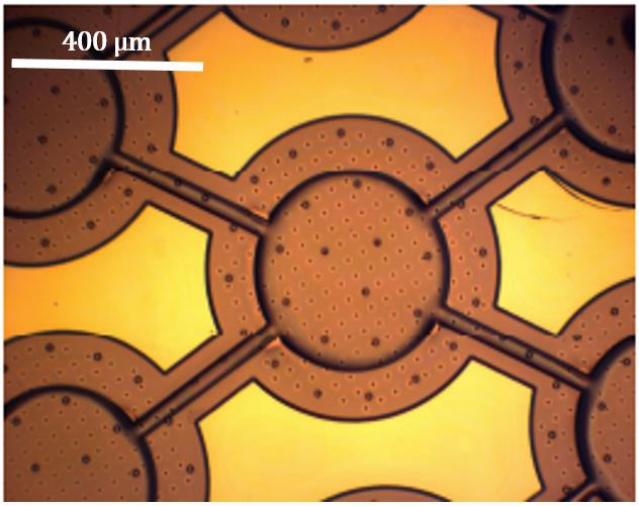

Figure 3-6 - Sacrificial layer after lithography for structural layer

(7)

The second to last step involves building the structural layer of the cMUT. First, the layer is patterned with photoresist (Figure 3-6), and then it is deposited through nickel electroplating. Two nickel plating methods are shown below:

Table 3-4 - Nickel electroplating parameters

Previous Method	**New Method**
"Technic Nickel Sulfamate Semi-bright Ready to Use" *Contains*: nickel sulfamate (80 g/L), nickel bromide (40 g/L), and boric acid (30 g/L) Temperature: 54 C provided by hotplate Current density: 5mA/cm^2 Expected deposition rate: 100 nm/min Continuous filtration	*Nickel Sulfamate from Technic* *Contains*: nickel sulfamate (80 g/L), nickel bromide (40 g/L), and boric acid (30 g/L) Temperature: 54 C provided by immersion heater Air bubbling Current density: 15mA/cm^2 Expected deposition rate: 310 nm/min Continuous filtration

As shown in Figure 3-7 the fabrication process of the cMUT is almost finished.

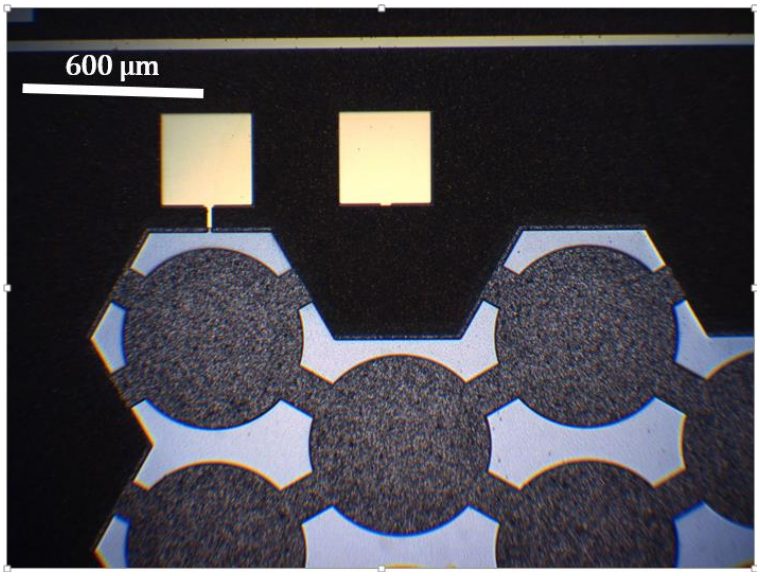

Figure 3-7 - Structural layer after nickel electroplating

(8)

The final critical step involves removing the sacrificial layer of the cMUT. This is done by placing the device in a copper wet etch solution, which is a 1:1:18 mixture of Acetic Acid, Hydrogen Peroxide (30%), and water for 1 to 7 days. Afterwards, it is dried. The most recent drying method involved critical point drying, which is described in more detail in the subsequent section.

3.2 Critical Point Drying

An important failure mechanism in surface-micromachined devices is the adhesion that occurs between released structures and the substrate. During processing, adhesion is likely to occur when a suspended member is exposed to an aqueous rinse and dry cycle [9-10]. Considering the sacrificial layer of these devices is approximately a few microns thick, the capillary forces that develop during the dehydration step are strong enough to cause the diaphragm to collapse and remain pinned to the substrate. According to Mastrangelo *et al* [11], this mechanism, known as stiction, will develop once certain conditions are present. First, the stiffness of the suspended structure must not be strong enough to overcome the strong capillary forces, thus causing it to

collapse. Second, if both surfaces come into contact, then the intersolid adhesion must be stronger than the restoring force of the elastic member, thus causing it to remain pinned to the substrate. A solution that reduces the likelihood of stiction can be found in critical point drying.

As part of the fulfillment of this thesis, a critical point dryer (CPD) was installed at the TMNF. This process first involved analyzing the pipe network within the device. Then components had to be purchased and constructed to supply power and collect exhausts such that the device could operate according to manufacturing standards. A schematic illustrating the device's operating procedure is shown in Figure 3-8.

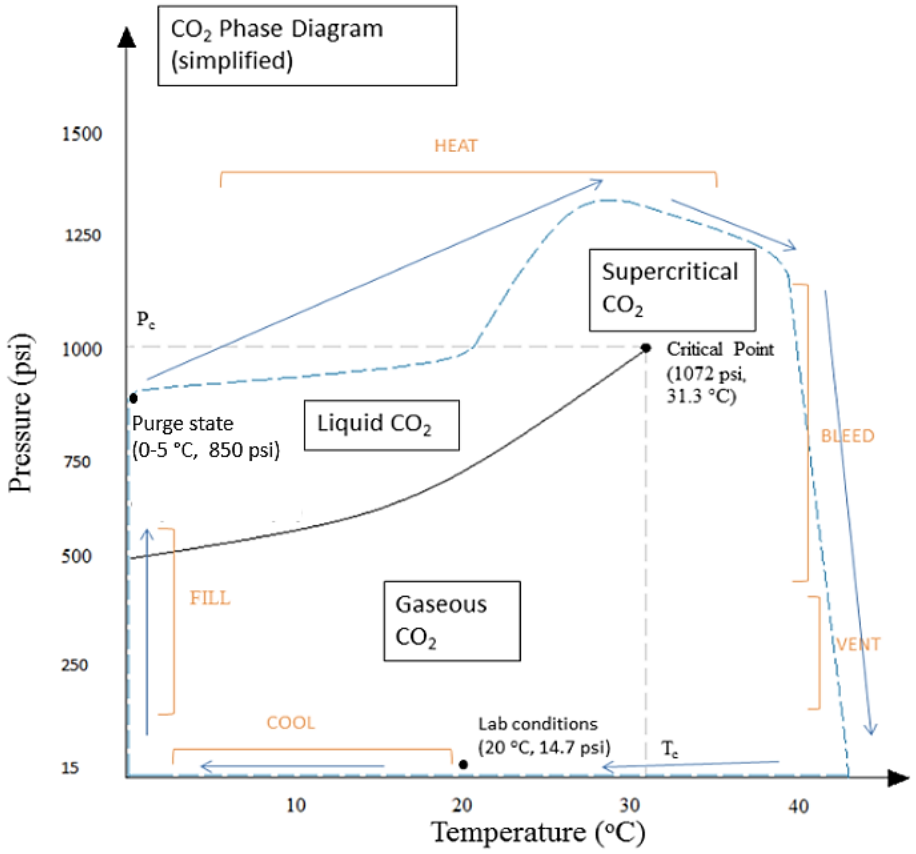

Figure 3-8 - Simplified phase diagram illustrating critical point drying as a path through the pressure-temperature plane

Initially, the devices are in a die holder submerged in a chamber filled with methanol. The CPD first cools the chamber to 0 °C so that the chamber could be filled with liquid carbon dioxide (CO_2). As it is being filled, the methanol is slowly purged until it is no longer present. Once filled with CO_2, the CPD raises the pressure then the temperature of the chamber until the fluid reaches a supercritical state. In other words, it is neither liquid nor gas, which significantly reduces the influence tension forces. Afterwards, the CPD gradually reduces pressure while maintaining a temperature above the critical point of CO_2 to ensure that the fluid enters a gaseous phase. In short, the CPD successfully dries the devices without passing through a liquid-gas transition.

An experiment was conducted to determine whether the CPD at the TMNF was more effective than a drybox, which is a low humidity environment. A while light interferometer, which measures surface deflection using an interface fringing technique, was used to examine cantilever beams dried using the two methods. As seen in Figure 3-9, there are more frequent fringes along the longer structures that were released in the drybox indicating that stiction had occurred; however, these fringes were not present on the structures of similar lengths that were dried in the CPD. Thus it was observed that the CPD structures were not stuck down. Consequently, results showed that critical point drying could be incorporated in the fabrication process instead of low humidity drying in order to reduce stiction during the release step of the devices.

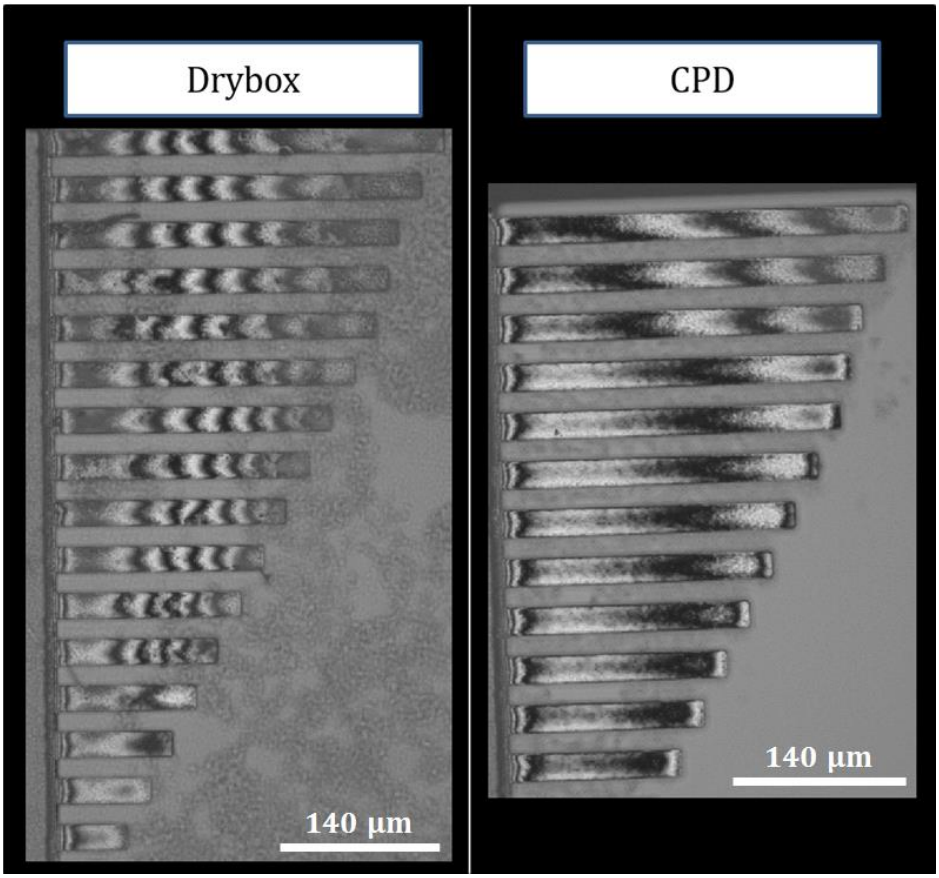

Figure 3-9 - Released structures dried using a drybox and a critical point dryer. The test structures have identical lengths. The long drybox structures are stuck down, but they are released when CPD is used.

3.3 Electroless Nickel Plating

As part of the fulfillment of this thesis, research was done on electroless nickel plating. The goal was to explore the possibility that it could be used to replace the current electroplating step that builds the structural membrane of the cMUTs. In conventional plating, metal ions are deposited by use of an externally supplied current. The current density on the object being plated (i.e. the cathode) determines the amount of metal that gets deposited on its surface. On the other hand, in electroless plating, a reducing agent in an aqueous solution causes the catalytic reduction of a metallic ion which then gets deposited on the surface of interest. Unlike electroplating, electroless plating does not require any externally applied current. Instead, factors such as the temperature and pH level of the bath play a more significant role on the deposition rate of the metal [12]. According to Krishnan *et al*, the coatings obtained through electroless nickel plating

are of uniform thickness all over the object being plated. Furthermore, the physical and mechanical properties of the deposit are uniform at all thicknesses. For this research, the electroless plating process materials were purchased from Uyemura International Corporation. These include the NPR-18CM solution, which has the nickel ions and ammonium salts, the MCT-14 solution, which is an activator mainly composed of Sulfuric Acid (~10%) and water. The testing was split into two major components.

The first step was to determine appropriate plating parameters. An experiment was conducted to determine whether it would be necessary to treat the surface of a specimen before plating nickel onto it. For this process, using the NSC-3000 sputter tool, a thick layer of copper (~3 μm) was deposited onto the glass slides to mimic the sacrificial layer of the cMUT. Then, slides were placed in an oxide etch (MCT-14) that would remove any oxide layer that may be present on the surface. Finally, the samples would be immediately transferred to the plating solution. Through an iterative process, an oxide etch for two minutes with slight agitation proved to be effective to prepare the surface for plating. Manufacturer recommendations were followed in setting the temperature of the MCT-14 solution. A stir bar was inserted in the solution to prevent small bubbles from forming on the surface during plating. The results of this experiment determined that a rotational speed of 125 RPM for the stir bar as well as a solution temperature of 80°C were preferable for plating nickel on the slides. From this experiment a standard operating procedure was produced and added to the library of deposition processes at the TMNF. The testing setup can be seen in Figure 3-10.

Figure 3-10 - Electroless Nickel Plating Setup

The second component was to determine whether the process was compatible with the cMUT process. Consequently, glass slides with evaporated Ti/Cu underwent an extra lithography step with AZ9260 photoresist to pattern the structural layer. Sputtering was abandoned as it resulted in poor adhesion between the Ti/Cu layer and the glass (Figure 3-11).

Figure 3-11 - Delaminated film after electroless nickel plating

After the plating process completed, none of the features from the lithography were present, indicating that the NPR-18CM solution had removed the photoresist. Consequently, the lithography step was modified by incorporating a postbake after the exposure to improve the chemical resistance of the photoresist. The post exposure bake lasted approximately 5 minutes at 150 °C. Then, the plating step was performed. Finally, the photoresist was stripped from the slides. As seen in Figure 3-12, the features that were patterned from the lithography were still present, indicating that the process improved the compatibility of the photoresist with the cMUT process.

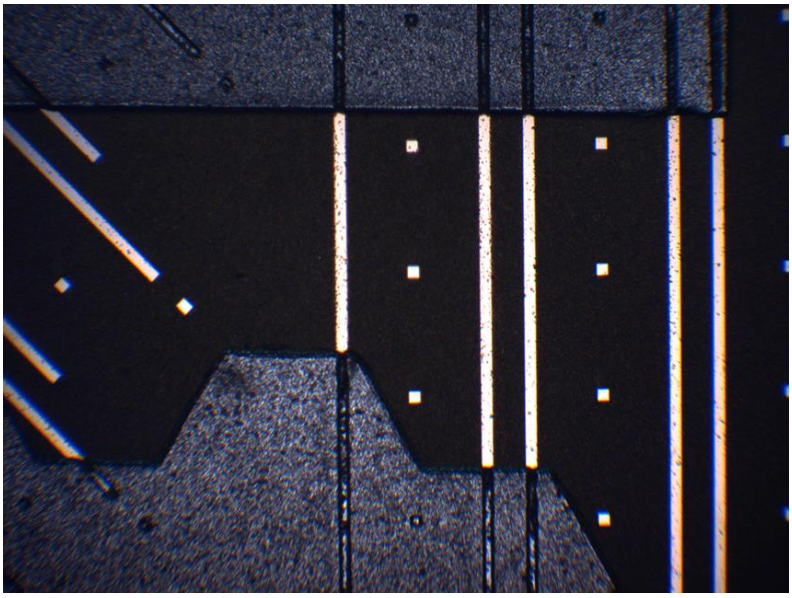

Figure 3-12 - Slide after electroless nickel plating and liftoff. Gray regions with a rough looking surface are part of the nickel layer

4 Methods

The cMUT's initial design was meant for operation at atmospheric pressure. A model of the device's structure allows a few conjectures to be made regarding its dynamic behavior at lower pressures. For instance, the damping ratio is likely to decrease, as less air will be present to dampen the oscillation of the membrane. However, it was still unclear how accurately the modeling would reflect cMUT performance at these lower pressures. In an effort to develop a better understanding of the system's behavior at lower pressures, a few tests were performed. Two cMUTs with different structural and sacrificial thicknesses were studied in an effort to gain

some insight on how significantly these dimensions influence the mechanical behavior of the system (Table 4-1).

Table 4-1 - Dimensions of cMUTs that were tested

	Chip 7 – fabricated 2012	**Chip 4 - fabricated 2016**
Structural thickness	8.5 µm	3.7 µm
Sacrificial thickness	5 µm	2.2 µm

4.1 Experiment Setup

The experiment was set up such that the only factor that would influence the cMUT's dynamic behavior was the pressure of its environment. Consequently, the driving signal would remain constant throughout the entire process. A schematic of the entire setup can be seen in Figure 4-1.

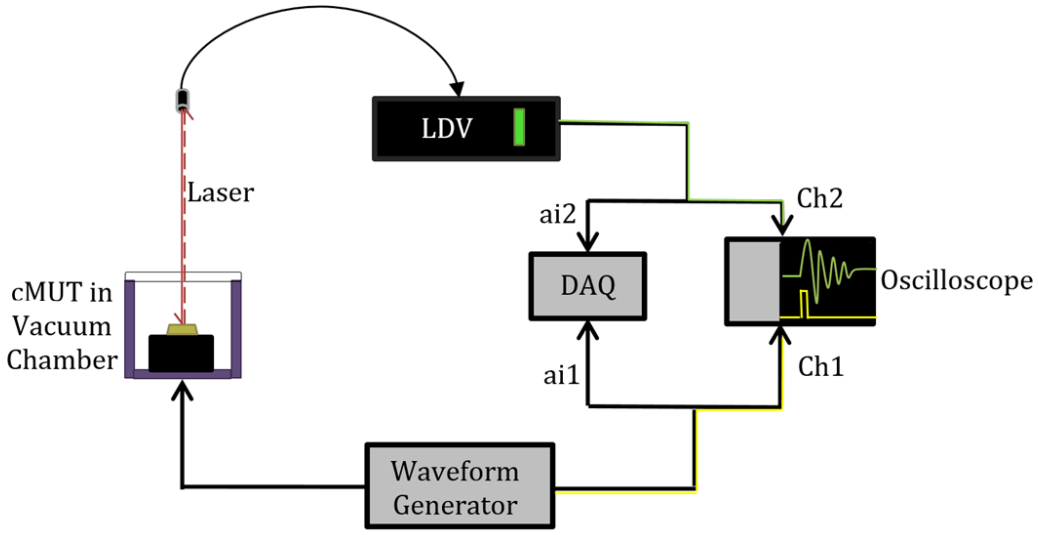

Figure 4-1 - Schematic of experiment setup with cMUT and LDV

- *Waveform Generator*: Generated a pulse that would cause the membrane to oscillate. The parameters of the pulse are found in Table 4-2.

- *LDV*: Emits a laser that measures the displacement of the membrane. The parameters for the LDV are found in Table 4-3.
- *Vacuum Chamber*: Controls the environmental pressure of the cMUT.
- *Oscilloscope*: Displays the input from the waveform generator as well as the output from the LDV to set the parameters for the Digital Acquisition System (DAQ). Channel 1 was used for the input and Channel 2 was used for the output. Time domain averaging (128 averages total) was used to reduce the noise that would be present in the output.
- *DAQ*: Records data points from the input and output signals at a certain sampling rate and stores them for future analysis.

Table 4-2 - Parameters of waveform generator

	Chip 7 - 2012	*Chip 4 - 2016*
Type of signal	Pulse wave	Pulse Wave
Repetition rate of pulse	10.0 Hz	10.0 Hz
Amplitude	10.0 V_{pp}	5.0 V_{pp}
Offset	+5.00 V_{DC}	+2.5 V_{DC}
Pulse Width	2.00 µs	2.00 µs

Table 4-3 - Parameters of LDV

	Chip 7 - 2012	*Chip 4 - 2016*
Displacement Decoder	50 nm/V	50 nm/V
Tracking Filter	Fast	Fast
Displacement BW	2 MHz	2 MHz

A visual of the test setup can be seen in Figure 4-2.

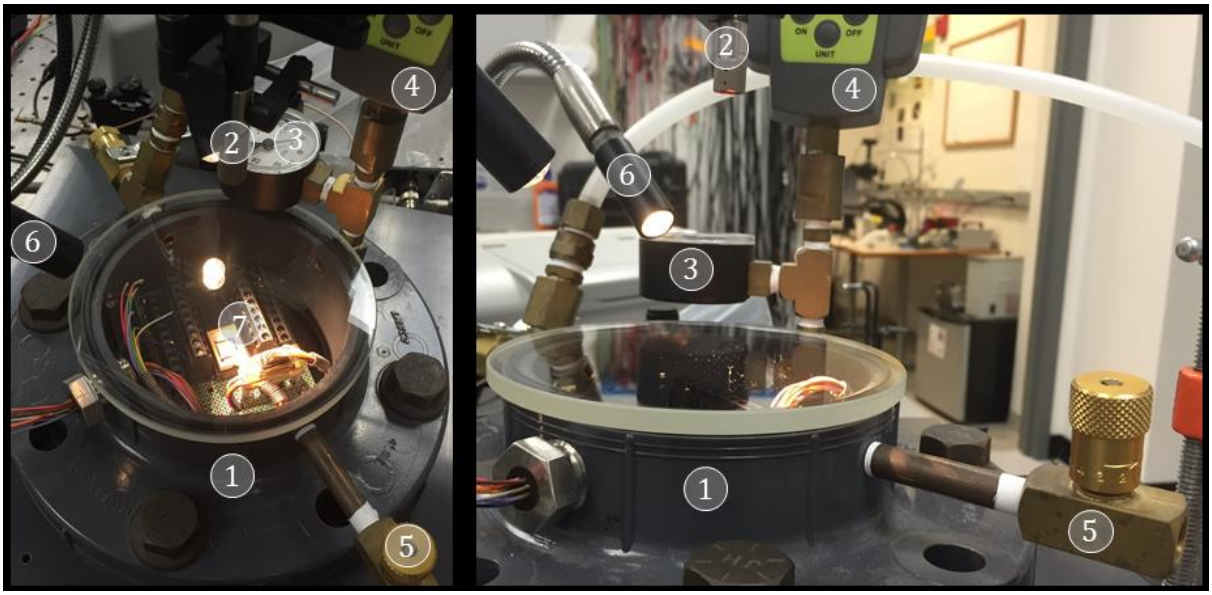

Figure 4-2 – Vacuum chamber with cMUT and pressure gauges

Table 4-4 - Components of vacuum chamber

1. Vacuum chamber	2. Laser head	3. Analog Pressure Gauge
4. Digital Pressure Gauge	5. Needle valve	6. Lamp
7. cMUT		

Two pressure gauges had to be used to increase the accuracy of the measurements. A rotary vane pump (Galileo Vacuum Tec Vacsound D12) was used to decrease the pressure within the vacuum chamber. At the lowest pressure, the analog pressure gauge read -30 inHg (or 30 inHg below atmosphere), which is indicative of a "perfect" vacuum. However, the analog gauge does not have sufficient resolution at low pressures, therefore the reading on the digital pressure gauge, which was ~1Torr, was used at low pressure. This pressure is low enough to simulate the atmospheric settings of a Martian environment, which is approximately 4.5 Torr at the surface. In order to gradually increase the pressure of the chamber, a needle valve was used. The goal was to measure the response of the cMUT at evenly spaced pressure settings. For simplicity, the major tick marks of the analog pressure gauge were used. During testing, the digital pressure

gauge stopped responding to changes in pressure near the -25 inHg range, so the reading of the analog pressure gauge was used instead for the higher pressures.

The dynamic behavior of a single membrane was considered. It was assumed that the other membranes of the device would exhibit a similar behavior. Consequently, as seen in Figure 4-3, the element closest to the bonding pads was the only one analyzed throughout the experiment.

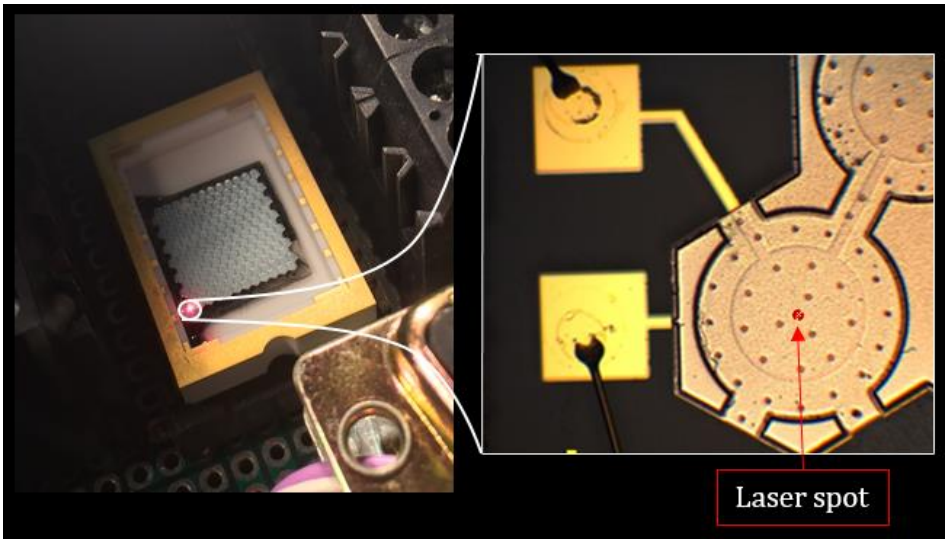

Figure 4-3 - cMUT element with laser spot on membrane

4.2 Data Acquisition & Analysis

This section describes the techniques that were used to gather data on the displacement of the membrane as well as the algorithms that were performed to analyze it. The latter makes use of a time domain as well as a frequency domain method to determine how consistent the results are. Finally, the data is compared to its expected model based on the LEM.

4.2.1 Data Acquisition

LDV measurements were recorded using two different methods. As shown in Figure 4-1, the data is sent to the oscilloscope and the DAQ. In certain instances, it was not possible to measure the resonant frequency of the output signal as the resolution of the oscilloscope was too low. Consequently, a LabVIEW VI (see Appendix B) was written to perform the same task as the

oscilloscope. The DAQ consisted of a NI PCI-6251 which has a maximum sampling rate of 1.25MS/s. Since the sampling rate of 1.25 MS/s could only be achieved through a single channel, the driving signal and the output signal were recorded at different times. Pre-triggering was implemented as well so that the entirety of the signal could be observed. This program was run numerous times to confirm that the consistency of the data that was displayed on the waveform graph. This information was stored in an array that would be copied in another VI (see Appendix C) that would record the output signal. The critical portion of this step was to ensure that the same parameters (i.e. pre-trigger samples, sampling rate, and number of samples) in both VI's were exactly the same. Through an iterative process, the sampling rate and number of samples per channel were manipulated until a reasonable output was displayed on the waveform graph. Another waveform graph that showed the ratio of the power spectra of both signals was used to ensure there wasn't much noise near the expected resonant frequency of the devices. Finally, the data was saved as a *.csv* file. It consisted of the driving signal, the output signal, and the transfer function of the system.

4.2.2 Data Analysis Using MATLAB

Since the process used to analyze the data at each pressure was similar, this section will focus on presenting how the data was analyzed at atmospheric pressure (chip 7). Once the time, voltage input, and voltage output data were imported into MATLAB, a few preliminary steps were taken. First, the input was squared. This is because the electrostatic force is proportional to the voltage squared. Then, the output was multiplied with the LDV's displacement decoder sensitivity so that the units of the output would be in nanometers. Finally, the ratio of the Fast-Fourier-Transform of the output and the squared input was computed; this new data set represented the output of the transfer function at various frequencies. Only the first half of the result is retained, as any data above the Nyquist Frequency would be redundant. Then, using the number of data points in the time array as well as the duration of the signal, it was possible to create a secondary array that would serve as the frequency domain of the transfer function, which now had units of nm/V^2. This process is described in (Appendix D).

As a final step, the steady state offset of the input and output signals was computed and subtracted from the originals so that the center of the waveform will be at zero. In order to compare the behavior the system to the LEM of a single transducer, the data was analyzed using a time-domain method and a frequency-domain method. The expectation is that both methods would compute similar Q factors and undamped natural frequencies.

4.2.2.1 Time Domain Method

To use this method successfully, the output signal should resemble that of a simple damped oscillator. As seen in Figure 4-4, a 10V wave with a width of 2μs caused the membrane to oscillate. Due to its stiffness as well the squeezing air molecules in the chamber, the oscillation peaks decayed exponentially. This behavior is modeled by the equation:

$$x = A_o e^{-\zeta \omega_n t} \tag{4}$$

where ζ represents the damping ratio and ω_n represents the underdamped natural frequency of the system. The goal was to estimate these parameters based on the cMUT's response.

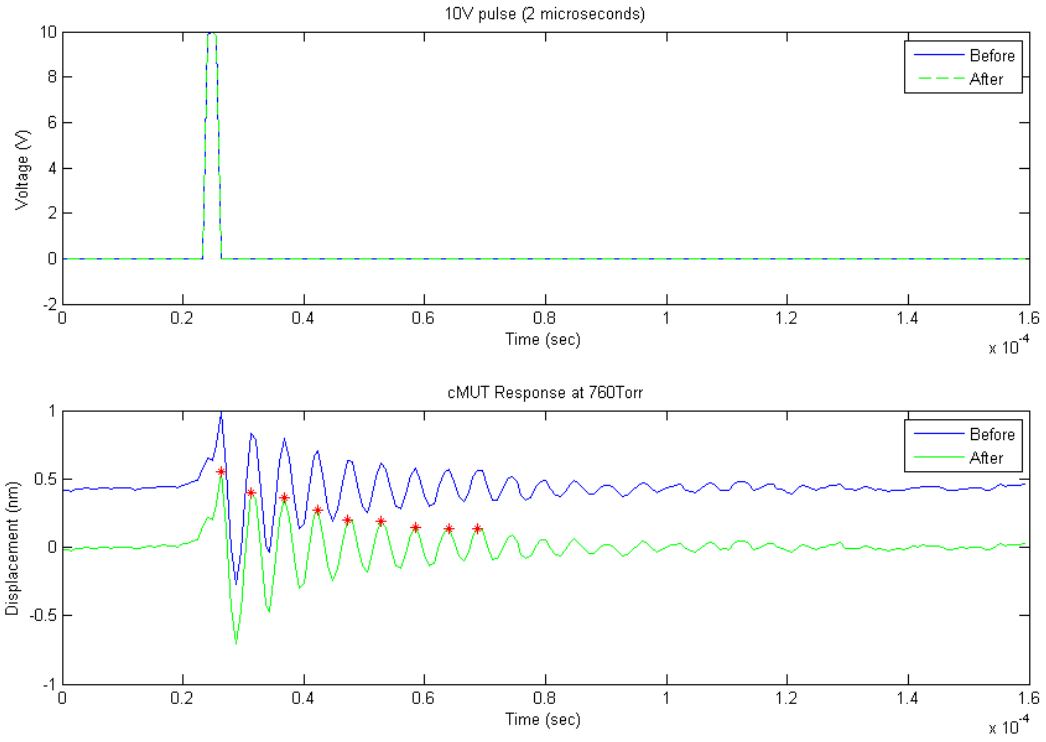

Figure 4-4 – Input and output signals at atmospheric pressure

The first step involved locating the peaks of the signal while keeping track of the times at which they occurred. The algorithm that performs this step is described in Appendix E. Essentially, it locates all the local maxima within a time range that occurred above a certain threshold. Then by implementing the log decrement method, it was possible to determine the damping ratio as well as the undamped natural frequency of the system. As seen in Figure 4-5, the calculated parameters accurately modeled the behavior of the data that was measured with the LDV.

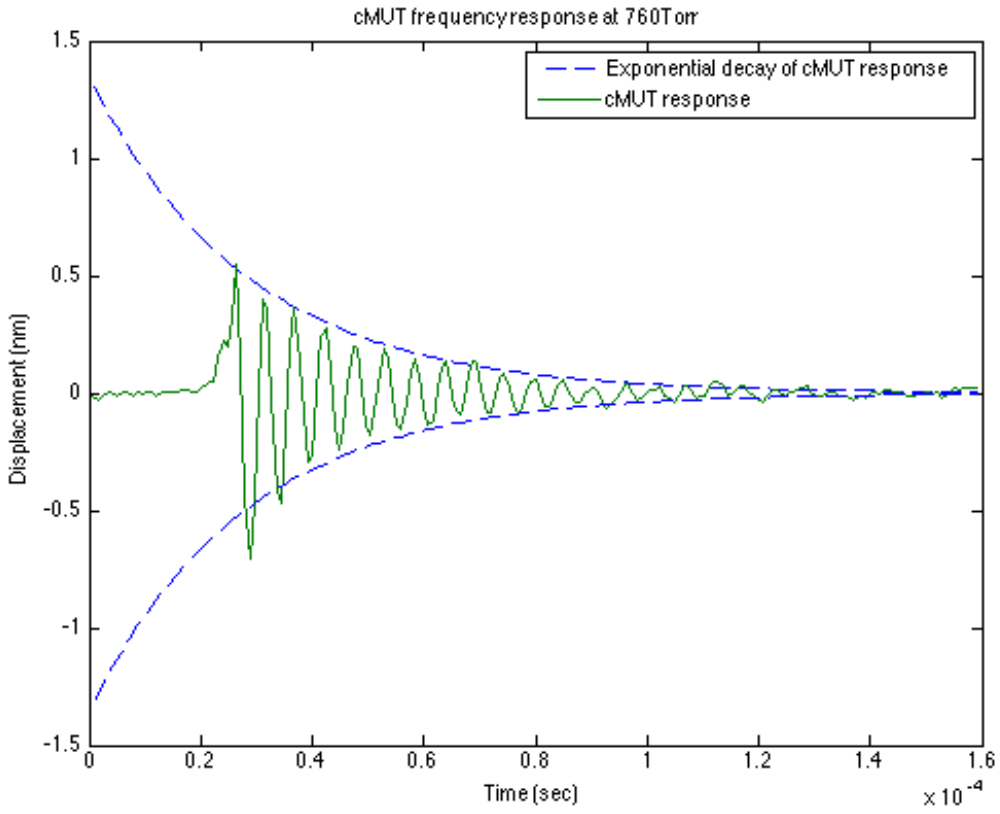

Figure 4-5 - Exponential decay of output based on calculated damping ratio and undamped natural frequency at atmospheric pressure

4.2.2.2 Frequency Domain Method

The frequency domain method could only be used under certain conditions. First, it was assumed that there would only be one peak near the expected resonant frequency. Second, the amount of noise near that frequency should be minimized to improve the accuracy of calculations. Finally, the resolution of the signal should be high enough such that there would be enough data points that could verify how well the calculated damping ratio reflects the actual behavior of the system. The procedure to calculate the damping ratio is described below.

1. Assume that the undamped natural frequency of the system occurs at the frequency with the largest output between 170 kHz – 190 kHz. This step was completed by inspection (Figure 4-6).

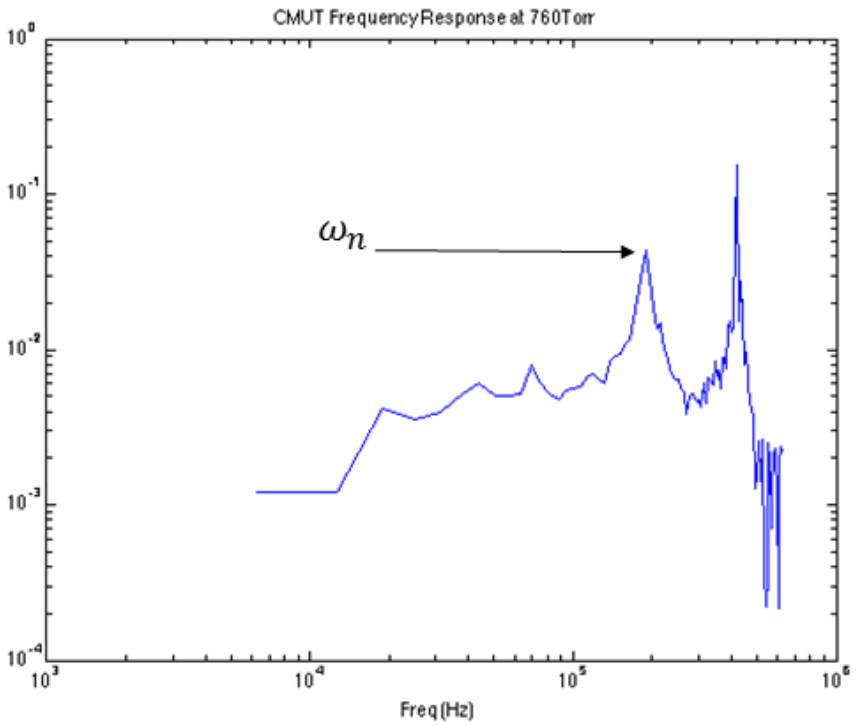

Figure 4-6 - Transfer function of the cMUT at atmospheric pressure. Characteristic frequency present at 187.5 kHz.

2. Through a simple algorithm described in Appendix F, store the frequencies in the vicinity of ω_n along with their output in an array.
3. Based on the damping ratio that was calculated using the time-domain method, make a conjecture that the damping ratio using the frequency domain method will be similar. Along with that, guess an initial value for the DC Gain, K_{dc}. The last step will involve figuring out which values best fit the data according to the following equation that describes a second order system:

$$H(s) = \frac{K_{dc}\omega_n^2}{s^2 + 2\zeta\omega_n \cdot s + \omega_n^2} \tag{5}$$

   Where $s = j2\pi f$ with f in Hz.
4. Set maximum and minimum limits for K_{dc} and ζ. Using an algorithm described in Appendix G, the best value for K_{dc} and ζ within the bounds are returned. This is done by minimizing the norm of the error between the data and model. As seen in Figure 4-7, the best estimates for K_{dc} and ζ are located at the minimum of the least squares map.

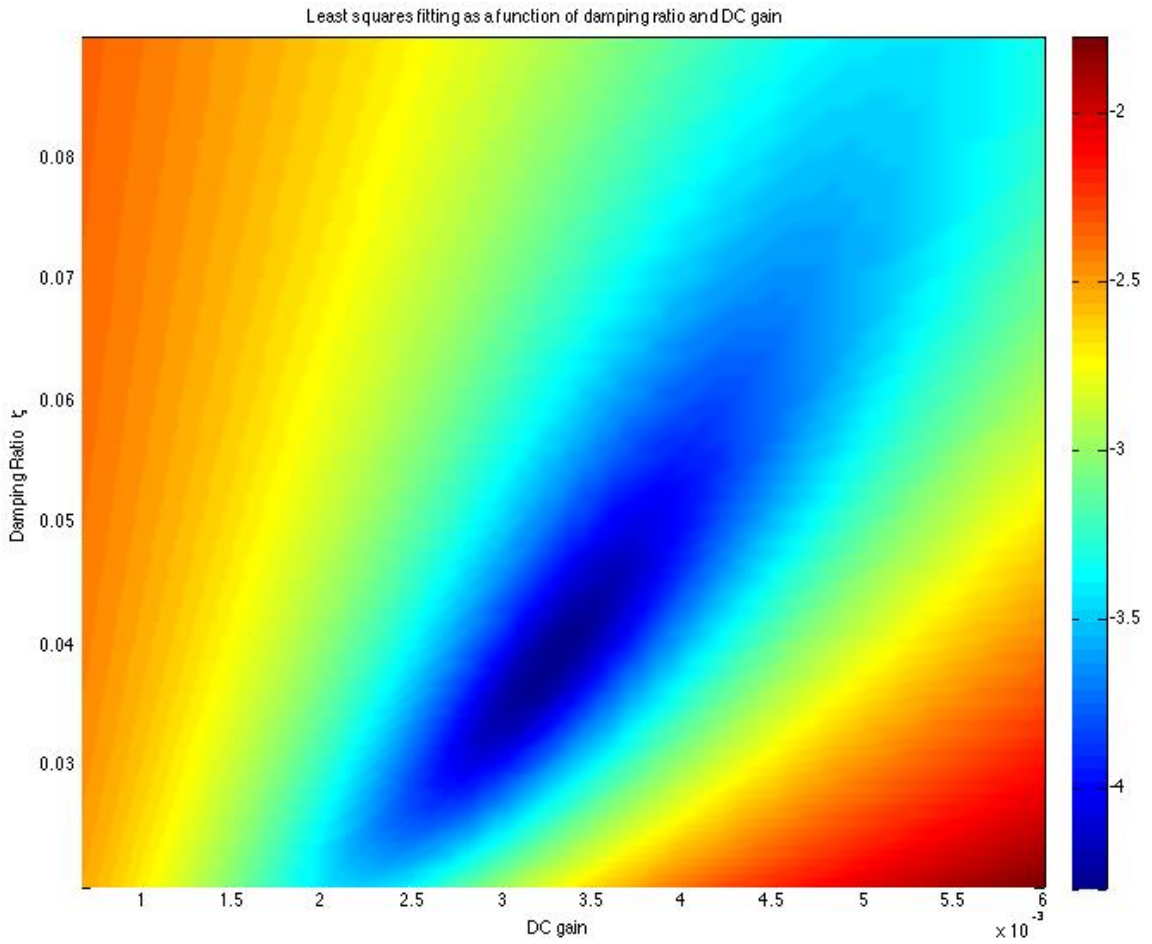

Figure 4-7 - Topological map showing where the smallest least squares fitting occurred based on $\boldsymbol{K_{dc}}$ and $\boldsymbol{\zeta}$

5. Finally, the parameters are plotted against the actual data. Through an iterative process, slight changes are made to the initial guess of ω_n, K_{dc}, and ζ until a reasonable match is found (Figure 4-8).

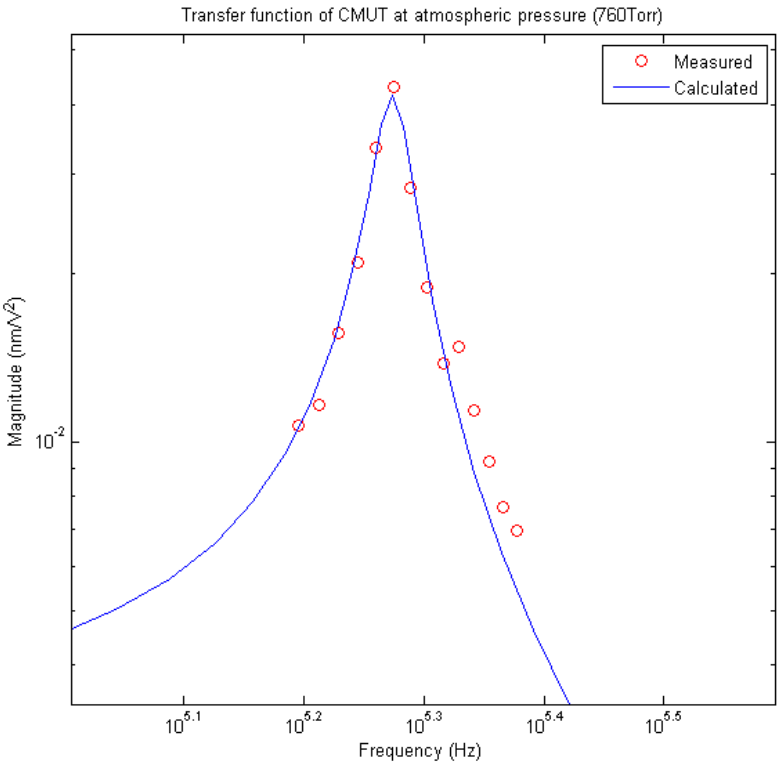

Figure 4-8 - Transfer function of cMUT showing how well calculated parameters fit the data

4.2.2.3 Frequency-Domain Method vs. LEM

The last step was to determine how well the LEM of a single transducer compared to the LDV measurements. In order to do so, certain parameters in the model were modified (code for the modeling can be found in [3]. First, the electrostatic spring was removed. Then, the pinhole size and the residual stress in the structural membrane were altered until the Q factor and resonant frequency at atmospheric pressure using the model were matched to the Q factor and resonant frequency measured using the time domain and frequency domain methods. Finally, density was computed as a function of pressure based on the ideal gas law. It was also assumed that viscosity remains constant as the pressure changes [13].

The last step involved extracting from the model the frequencies and magnitudes of the transfer function around the resonant frequency and seeing how well the model matched lab measurements. As seen, in Figure 4-9, there's an offset in the magnitude of the LEM relative to

the measured data. This discrepancy may be due to the fact that in the model the cMUT was driven with AC signal and not a pulse.

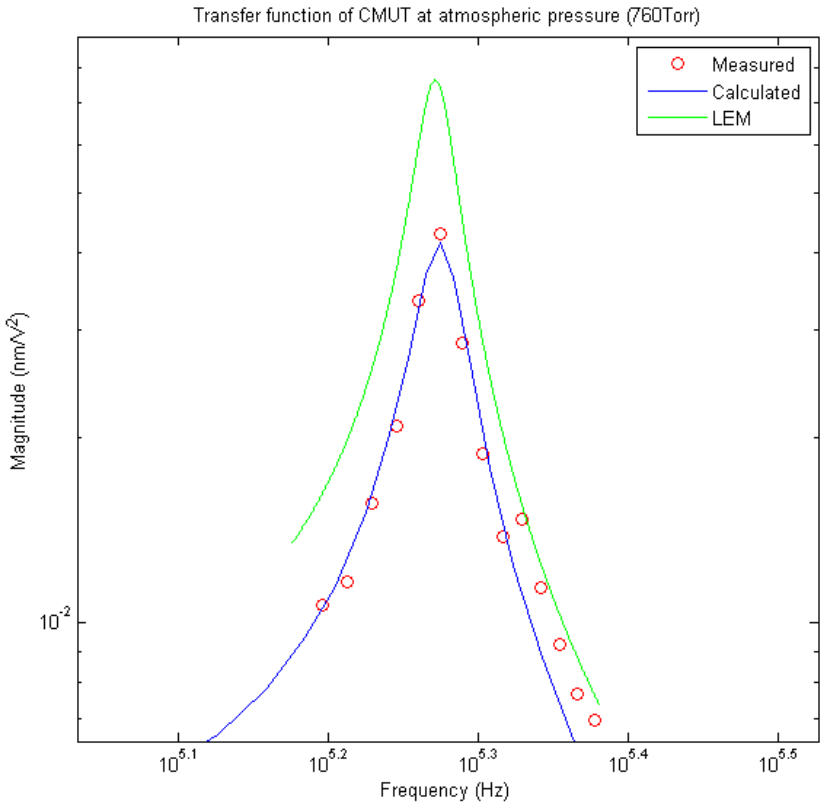

Figure 4-9 - Approximation of the cMUT's expected behavior based on LEM

5 Results

This section discusses the results from repeating the steps described in the previous section at various pressures. Special emphasis is placed on the natural frequency and the quality factor of both transducers that were tested.

5.1 Undamped Natural Frequency

One of the main challenges associated with the Time Domain Method was that it was mainly done by inspection. Since the output signal came from a pulse, the first peak of the signal was not considered as its magnitude was influenced by the width of the pulse. By inspecting Figure 5-1, there is a noticeable disturbance at t = 2μs. This is due to the fact that the pulse wave was 2

μs and thus was still driving the cMUT even after it had started to oscillate. Consequently, the log decrement method was only applied to subsequent peaks where the pulse wave was absent. Regarding the algorithm that was used to locate the peaks, it is slightly inaccurate, as it does not take into account noise that may be present in the signal. As seen in Figure 5-1, the exact location of the second peak is unclear. This phenomenon is even more evident at the third peak. By inspection, it can be deduced that the quality factor of chip 4 at 633 Torr is relatively low as there are very few noticeable peaks. Since the first one could not be used, the exponential decay was fit to the peaks that occurred below the time axis. Furthermore, it proved challenging to determine the correct parameters that could fit all peaks that were observed due to all the noise.

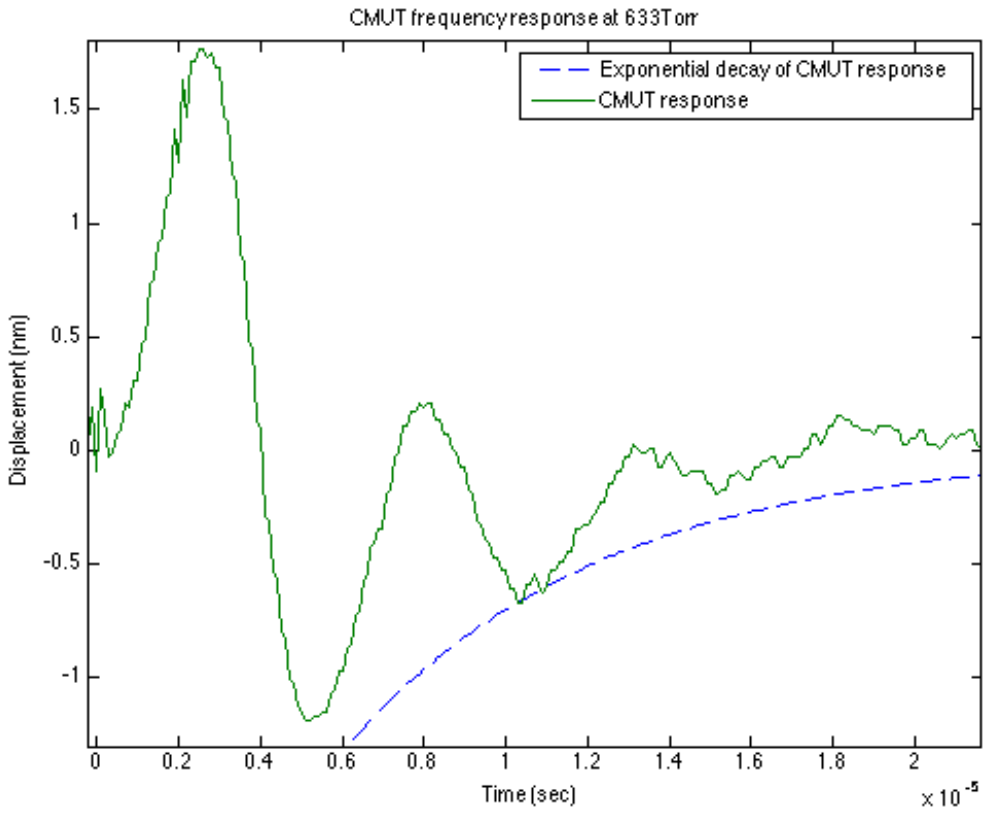

Figure 5-1 - Response of Chip 4 - 2016 at 633 Torr

While this technique was relatively straightforward, it could not be used at the lowest pressure that was measured during testing. For instance, at 1 Torr, the behavior of the cMUT was not representative of a simple damped oscillator (Figure 5-2). This may be due to coupled oscillator

behavior as it interacts with other elements in the array. Consequently, only the frequency-domain method was used to determine the damping ratio and undamped natural frequency.

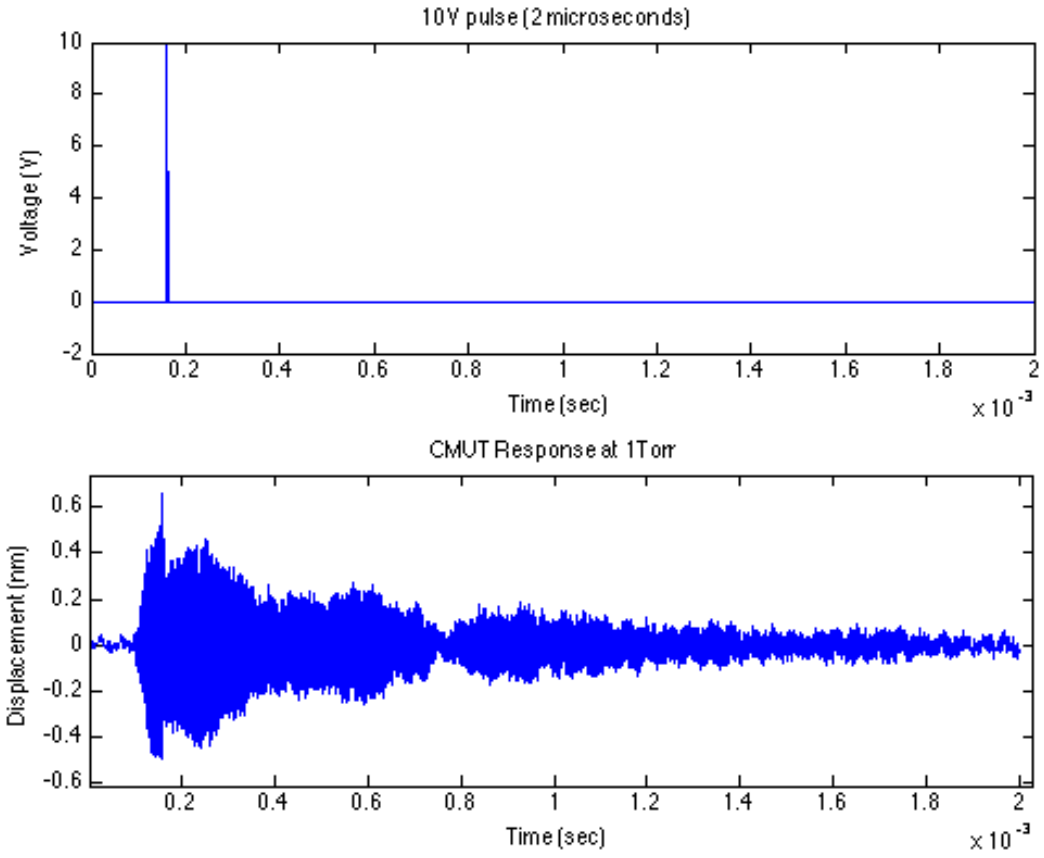

Figure 5-2 - Input and output signal of cMUT at 1 Torr

As seen in Figure 5-3, the undamped natural frequency of chip 7 seems to remain constant as the pressure of the system decreased. The results through the LEM agree mostly with the Frequency Domain method, with the exception of the lowest pressure (~1 Torr) where it suggests that the natural frequency of the system should have decreased. By averaging the measurements from the Time Domain and Frequency Domain methods, it can be deduced that the resonant frequency of chip 7 is 183 ± 4.5 kHz at all pressures.

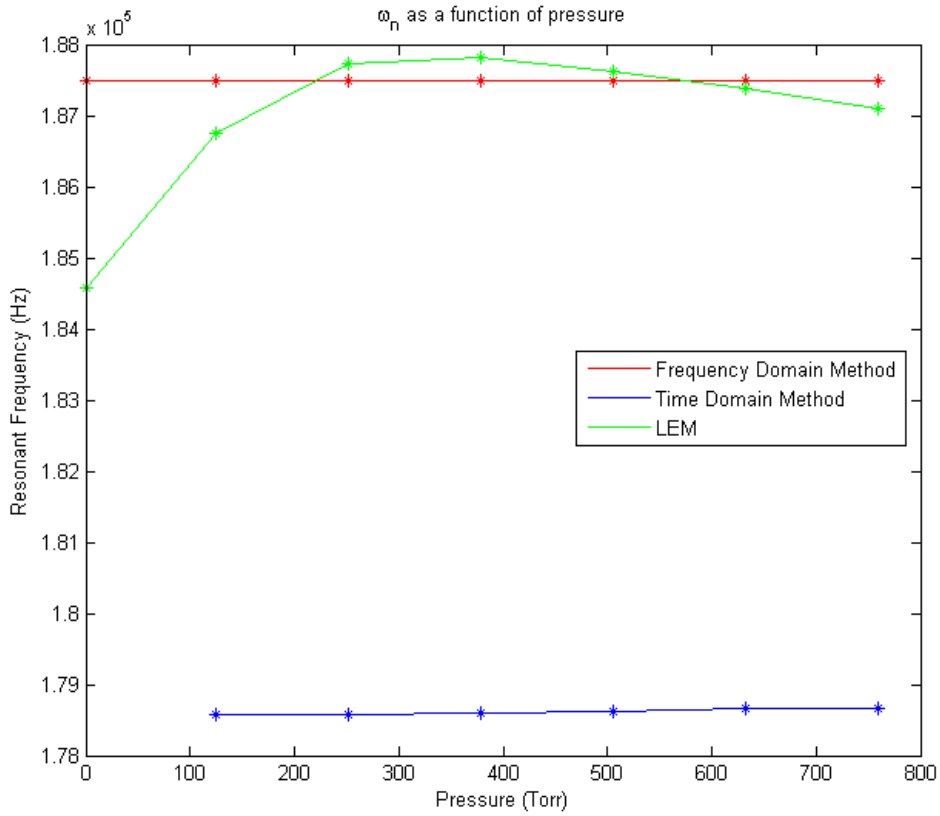

Figure 5-3 - Undamped natural frequency as a function of pressure (Chip 7)

By inspecting Figure 5-4 an immediate contrast relative to Chip 7 is the decrease in the undamped natural frequency of Chip 4 from 204 kHz to 116 kHz. Another clear discrepancy between the Time Domain Method and the other two is that the proportional relationship between the resonant frequency and the pressure is less evident. Nonetheless, data gathered from all three methods agree that in the thinner cMUT the compliance of the cavity played a more significant role in determining the resonant frequency of the system.

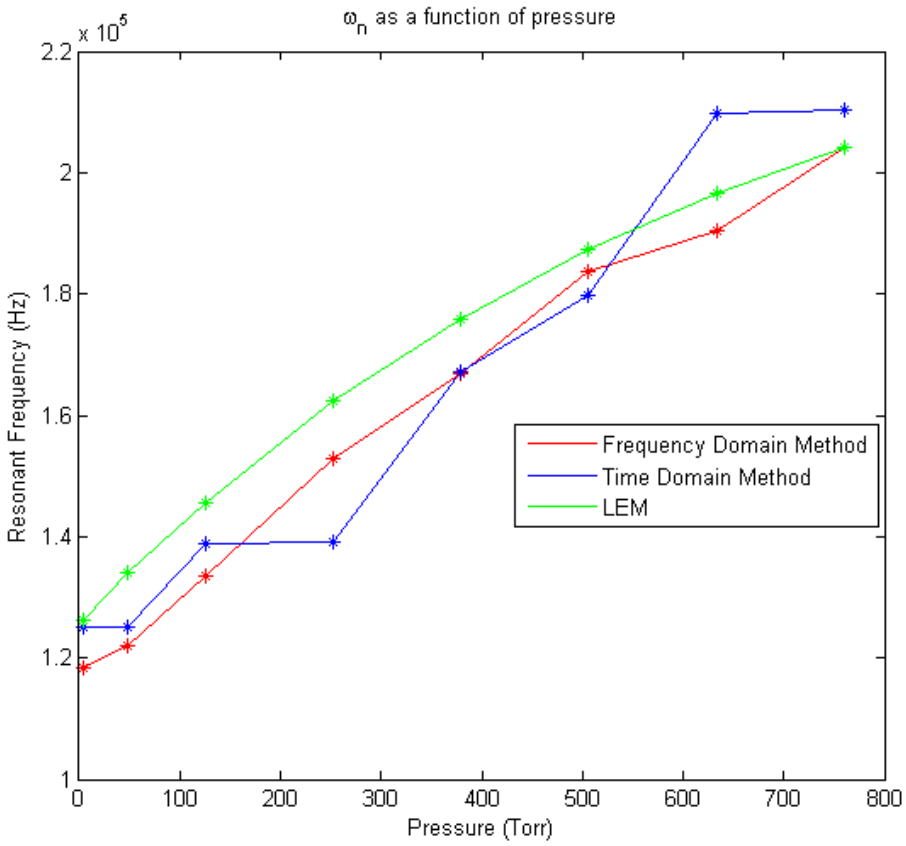

Figure 5-4 - Undamped natural frequency as a function of pressure (Chip 4)

5.2 Quality Factor

As described in section 2.2.4, the modeling used by our group to estimate the performance of the cMUT in a Martian atmosphere showed a very narrow band output near the resonant frequency. In other words, there was an increase in the quality factor. As seen in Figure 5-5, a similar outcome was seen in the LDV measurements. Essentially, as the pressure in the system decreased, the damping due to the viscosity of the air was much less significant, allowing the membrane to oscillate a lot more as the pressure reduced. The data indicates that there is a nonlinear relationship between pressure and the Q factor. For chip 7, it is important to point out that the Q factor calculated using LEM at the lower pressures is much larger than what was measured during testing. This can be attributed to the LEM not taking into account other damping mechanisms that become more relevant at low pressures. For instance, there may be some internal structural damping due to dislocations in the membrane, or loss of energy due to structural vibrations transmitted through the anchors and out into the bulk.

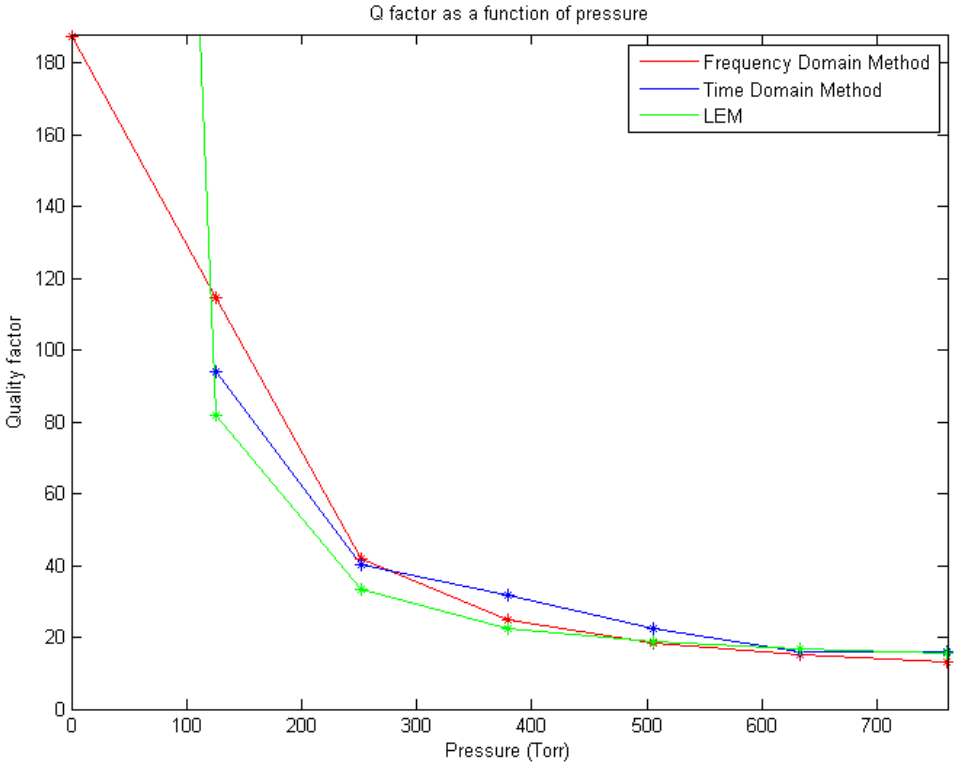

Figure 5-5 - Quality factor as a function of pressure (Chip 7)

As seen in Figure 5-6, with pressures above 50 Torr, all three methods that were used to estimate chip 4's performance agree very well; however, once again, LEM estimated a larger Q factor at the pressure of the Martian atmosphere.

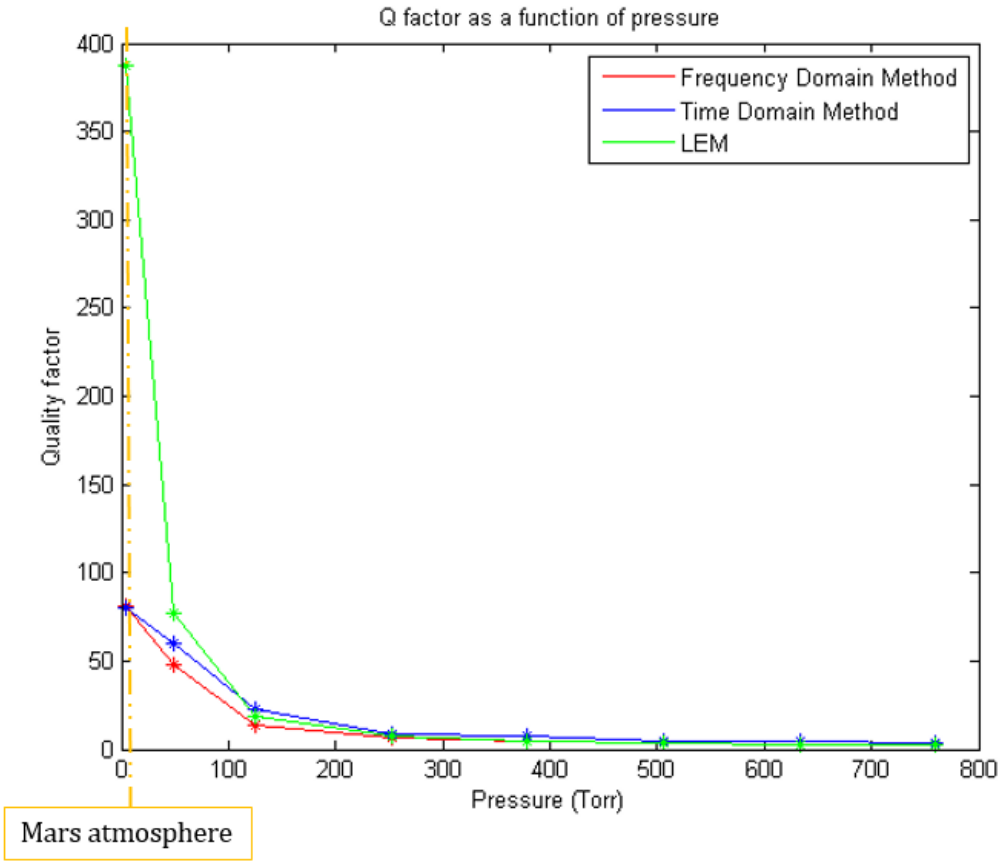

Figure 5-6 - Quality factor as a function of pressure (Chip 4)

6 Conclusions

In this chapter the contributions made to research made on cMUTs are presented. Additionally, a section describes future efforts that should be considered towards building a device that would work in a Martian environment.

6.1 Contributions

One of the most significant insights from this research came from the analysis of the undamped natural frequency of the system. Essentially, by performing tests on two cMUTs that have different sacrificial and structural thicknesses, it was possible to show two particular scenarios. In the first one the stiffness of the membrane was high enough that the resonant frequency remained unchanged as the pressure decreased. In the second one, where the cMUT

had a thinner membrane, the compliance of the cavity played a larger role in determining the resonant frequency of the system. Thus the resonant frequency dropped at lower pressures. This serves as evidence that an optimal way to decrease the resonant frequency of the system is by reducing the thickness of the sacrificial and structural layers of the device.
Another contribution made regarding the modeling of the devices was the validity of the LEM. Essentially, given the appropriate parameters, LEM can accurately estimate the quality factor and the resonant frequency of the cMUTs. That said, it becomes unreliable at calculating the former when the pressure of the system decreases below 50 Torr. Consequently, this opens up the opportunity to conduct research on other dampening mechanisms that could be included in the model for scenarios where the pressure becomes less significant.

Finally, contributions were made to the techniques that could be used to fabricate cMUTs. For instance, critical point drying is a very useful tool that can be used to release thin devices. Along with that, there is the possibility of obtaining devices with a more uniform thickness across the wafer by using electroless nickel plating.

6.2 Future Work

With the results drawn from this research, there are three major components that have to be improved. First, the cMUTs should be fabricated with an even thinner structural membrane to see if an even lower resonant frequency could be achieved. Evidently, a thinner structural membrane will require a thinner sacrificial layer. Consequently, there is the possibility that Critical Point Drying would be inadequate at releasing the devices properly. Thus, research could be done towards using self-assembled monolayers instead as they could be more effective at reducing stiction. In order to achieve a more uniform nickel thickness, there should be efforts made at creating a test setup for the electroless nickel plating that is compatible with the size of the cMUT wafer. If successful, this process could replace the current nickel electroplating process and would increase the likelihood that the structural membrane of cMUTs from a wafer would have similar thicknesses.

On the testing side, it is recommended that a better gauge pressure be used to accurately measure environmental conditions. This would minimize some of the uncertainty in the results gathered from this research as two different gauge pressures were used. Finally, the most important consideration would be to test the redesigned cMUT in a CO_2 filled environment with

a prototype anemometer. While the pressure of the Martian atmosphere is relatively low, it would be worth considering how much of an influence the properties of the medium affect the performance of the cMUT. This would also require developing a system model for the prototype anemometer.

References

1. Banfield, Don, and Richard Dissly. "A Martian sonic anemometer."*Aerospace Conference, 2005 IEEE*. IEEE, 2005.

2. Minchul Shin, Zhengxin Zhao, Paul DeBitetto, Robert D. White, "Micromachined ultrasonic Doppler velocity sensor using nickel on glass transducers", Sensors and Actuators A: Physical, Volume 208, 1 February 2014, Pages 37-49, ISSN 0924-4247

3. Shin, M. "MEMS Based Doppler Velocity Measurement System", Ph.D. Thesis, Tufts University, August 2012

4. Ergun, A. S., et al. "Fabrication and characterization of 1-dimensional and 2-dimensional capacitive micromachined ultrasonic transducer (CMUT) arrays for 2-dimensional and volumetric ultrasonic imaging." *OCEANS'02 MTS/IEEE*. Vol. 4. IEEE, 2002.

5. Hua, Hong, Yongtian Wang, and Dayuan Yan. "A low-cost dynamic range-finding device based on amplitude-modulated continuous ultrasonic wave." *Instrumentation and Measurement, IEEE Transactions on* 51.2 (2002): 362-367.

6. Konrad, W. "Underwater acoustic communications." *Communications Magazine, IEEE* 20.2 (1982): 24-30.

7. Cui, Jun-Hong, et al. "The challenges of building mobile underwater wireless networks for aquatic applications." *Network, IEEE* 20.3 (2006): 12-18.

8. Oralkan, Öincr, et al. "Capacitive micromachined ultrasonic transducers: Next-generation arrays for acoustic imaging?." *Ultrasonics, Ferroelectrics, and Frequency Control, IEEE Transactions on* 49.11 (2002): 1596-1610.

9. Gogoi, Bishnu P., and Carlos H. Mastrangelo. "Adhesion release and yield enhancement of microstructures using pulsed Lorentz forces." *Microelectromechanical Systems, Journal of* 4.4 (1995): 185-192.

10. Kim, Chang-Jin, John Y. Kim, and Balaji Sridharan. "Comparative evaluation of drying techniques for surface micromachining." *Sensors and Actuators A: Physical* 64.1 (1998): 17-26.

11. Mastrangelo, Carlos H. "Adhesion-related failure mechanisms in micromechanical devices." *Tribology Letters* 3.3 (1997): 223-238.

12. Krishnan, K. Hari, et al. "An overall aspect of electroless Ni-P depositions—a review article." *Metallurgical and Materials Transactions A* 37.6 (2006): 1917-1926.

13. White, Frank M. *Fluid Mechanics*. New York, NY: McGraw Hill, 2011. Print.

Appendix

A. cMUT Runsheet

RUNSHEET

Process Name: Nickel Surface Micromachining
Process Goal: Shear sensor run with glass substrate, Nickel structural layer 10 μm thick, Cu sacrificial layer 5 μm thick, and Cr/Au interconnect.
With Evaporated Cr/Au and Ti/Cu at Harvard
Author: Daniela Torres, Robert White, Jim Vlahakis, Zhengxin Zhao
Revision Date: February 19, 2016

Refer to SOPs: "Standard Lithography", "OAI Aligner", "Laurell Spinner", "NSC-3000 Sputter", "March RIE", "Copper Electroplating", "Nickel Electroplating", "LOR Liftoff".

Starting Substrates: 100±.2mm Soda Lime 550±50μm Thick DSP (60/40) W/Rounded Edges & Primary Flat Only.

Step Name	Parameters	Measurements/ Comments	Date Complete
1. Piranha Clean (REQUIRED – important for good results in #3)	Piranha clean starting substrates, 1:1 H_2SO_4:H_2O_2 (30%) by volume. 10 mins clean, 3 mins DI water x 2.		
2. O_2 Clean (REQUIRED)	200W, 120sec, 100% O_2 (~300 mT) in March RIE		
3. Lithography #1 Metal Mask v4	LOR20B: 500 rpm 4sec, 2000 rpm 45sec, 200C 5min softbake (dirty hotplate ***no tinfoil*,** with glass cover); AZ9260: 500 rpm 8 sec spread, 6000 rpm 60 sec spin, 115C 2 min softbake (clean hotplate with tinfoil), 30 sec exposure (hard contact), 2 min 20 sec develop in AZ400K:water 1:3, 2 x 2 DI water rinse, air gun dry	LOR20B: 2000 rpm = 2.0 μm AZ9260: 6000 rpm = ___ μm	
4. O_2 Descum	200W, 60 sec, 100% O_2 (280 mT) plasma descum in March RIE	Etch rate ~ 0.4 μm/min	

5. Cr/Au Evaporation	15 nm Cr/150 nm Au evaporated in EE4 ebeam evaporator at Harvard	Base pressure: Ti dep rate: Cu dep rate:	
6. Liftoff	Heated Remover 1165 in glass petri dish (covered) at 60C (80C hotplate temp) for > 3 hr. Transfer to fresh Remover, sonicate 5 minutes, DI water rinse 1000 mL beaker 3 mins x 2. Blow dry.	Measure thickness. Center: _____ nm Edge: _____ nm	
7. Lithography #2 "Anchor Liftoff" Mask v4 **IMPORTANT NOTE:** **This is mask #4 … when doing alignment it aligns to alignment mark #4!!!! (shear sensors)** **"Liftoff 2" Mask (cMUT)**	LOR20B: 500 rpm 4sec, 2000 rpm 45sec, 200C 5min softbake (dirty hotplate *no tinfoil*, with glass cover); AZ9260: 500 rpm 8 sec spread, 6000 rpm 60 sec spin, 115C 2 min softbake (clean hotplate with tinfoil), 30 sec exposure (hard contact), 2 min 20 sec develop in AZ400K:water 1:3, 2 x 2 DI water rinse, air gun dry	LOR20B: 2000 rpm = 2.0 µm AZ9260: 6000 rpm = ___ µm	
8. O_2 Descum	200 W, 60 sec, 100% O_2 (280 mT) plasma descum in March RIE		
9. Ti/Cu Evaporation	30 nm Ti/300 nm Cu evaporated in EE3 ebeam evaporator at Harvard	Base pressure: Ti dep rate: Cu dep rate:	
10. Liftoff	Heated Remover 1165 in glass petri dish (covered) at 60C (80C hotplate temp) for > 3 hr.	Measure thickness. Center: _____ nm	

	Transfer to fresh Remover, sonicate 5 minutes, DI water rinse 1000 mL beaker 3 mins x 2. Blow dry.	Edge: _____ nm	

11. Lithography #3 "Anchor Plate" Mask v3 (shear sensor) Or "Liftoff 2" mask (cMUT) **IMPORTANT NOTE:** **This is mask #2 … when doing alignment it aligns to alignment mark #2.**	HMDS/AZ9260 500 rpm 8 sec spread, 3000 rpm 60 sec spin, 120C 3 min softbake, 35 sec exposure (hard contact), 5 min develop in AZ400K:water 1:3, 2 x DI water rinse, air gun dry	Measure resist thickness: _____ μm (expect 6 μm)	
12. O_2 Descum	200 W, 60 sec, 100% O_2 (280 mT) plasma descum in March RIE		
13. Copper Electroplating	Plate on thick Cu (filter). See Cu plating SOP. 0.8M $CuSO_4$, 1.5M H_2SO_4, 80 ppm Cl^-, 20°C, 5 mA/cm^2 results in ~130 nm/min. 2 x DI water rinse. Wafer area 78 cm^2. So 390 mA gives ~5mA/cm^2. Shear sensor: Plate for 30 minutes. Target total Cu thickness 5 μm. cMUT: Choose time for desired thickness (~130 nm/min). *Stop deposition after half the expected dep time. Measure Cu thickness, and adjust length of remaining time accordingly.*		
14. Strip Photoresist	5 minute acetone soak, 2 min IPA, 2 min x 2 water, air dry,		
15. O_2 Descum	200W, 120sec, 100% O_2 (300 mT) in March RIE		

16. Measure Cu	DekTak Cu thickness	Total Ti/Cu/CU thickness:	
17. Lithography #4 "Structure" Mask (cMUT)	HMDS/AZ9260, 300 rpm 10 sec spread, 1000 rpm 60 sec spin 120C 4 min softbake (hotplate #1 with tinfoil and glass cover), 35 sec exposure hard contact, 5 min develop, AZ400K:water 1:3, 2 × 2 DI water rinse, air gun dry.	Measure resist thickness: _____ μm (expect 12 μm)	
18. O_2 Descum	200W, 60 sec, 100% O_2 (280 mT) plasma descum in March RIE		
19. Copper oxide etch	Etch copper oxide off in 10 % by volume sulfuric acid in water, 30 second dip, then 1 minute DI water rinse, and immediately into nickel plating solution.		
20. Nickel Electroplating	Plate on thick Ni. See Ni plating SOP. NICKEL SULFAMATE SEMI BRIGHT RUT MECHANICAL AGITATION, 50C (hotplate front panel temp for large tank = 180 C), 5 mA/cm^2 results in 100 nm/min. Structure mask has an area of 32 cm^2 (does not include edges or edge rectangles for both shear sensor and cMUT). Use 160 mA to achieve 5 mA/cm^2. Target thickness 10 μm (100 mins) for shear sensor, 5 um (50 mins) for cMUT. May want to stop half way and measure on DekTak. Uniformity problems can exist – rotating 180^o halfway through might be good.		
21. Strip Photoresist	10 minute acetone soak, 5 min IPA, DI water spin, spin dry.		
22. Measure Ni	DekTak Ni thickness at 5 points	Ni thickness: Flat (bottom):	

		Center: Top: Left: Right:	
23. Protect wafer	Spin on HMDS/AZ9260 at 3000 rpm, softbake 120C, 4 mins.		
24. Dice wafer	MA dicing saw – dice into individual dies. Die size (center to center on cuts = 10.1 mm)		
25. Strip Photoresist	10 min acetone soak, 5 min IPA, 5 min x 2 water. Blow dry each chip carefully (place on towel, blow straight down)		
26. O_2 Clean	200W, 120 sec, 100% O_2 (280 mT) plasma clean in March RIE		
27. Copper Wet Etch (Release)	1:1:18 CH_3COOH: H_2O_2: Water 1 day, 10min x2 DI water rinse, IPA 10 min, Methanol 30 min,		
28. Dry	Option #1 : 2 hr dry in drybox at reduced relative humidity Option #2: Tousimis critical point drier.		

B. LabVIEW VI to record input signal

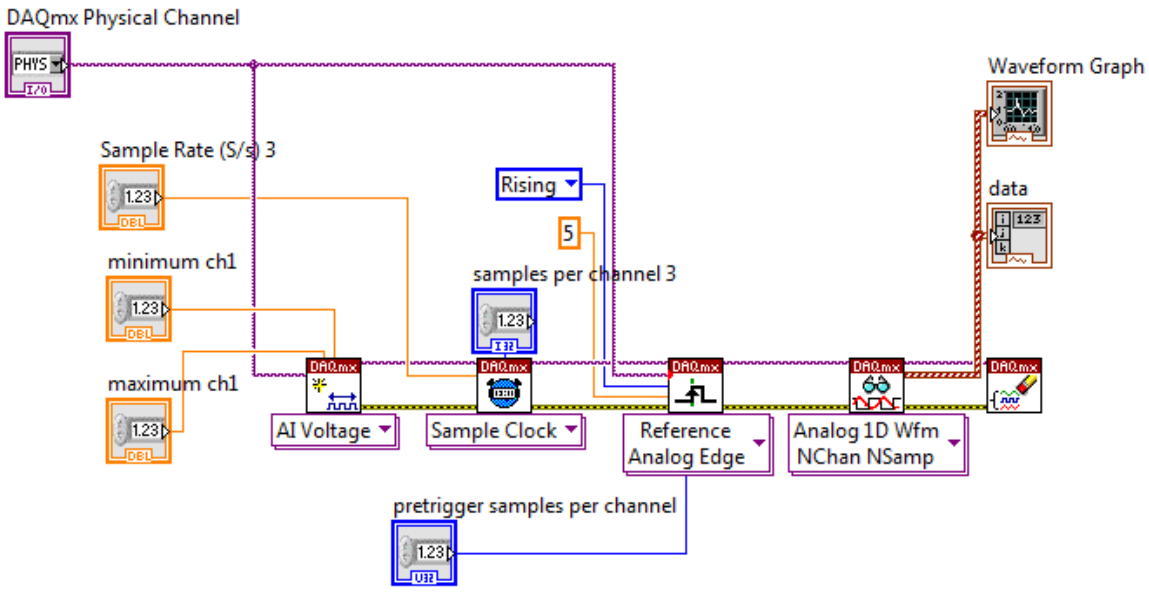

Figure 6-1 - LabVIEW VI that records the input signal

C. LabVIEW VI to record output signal

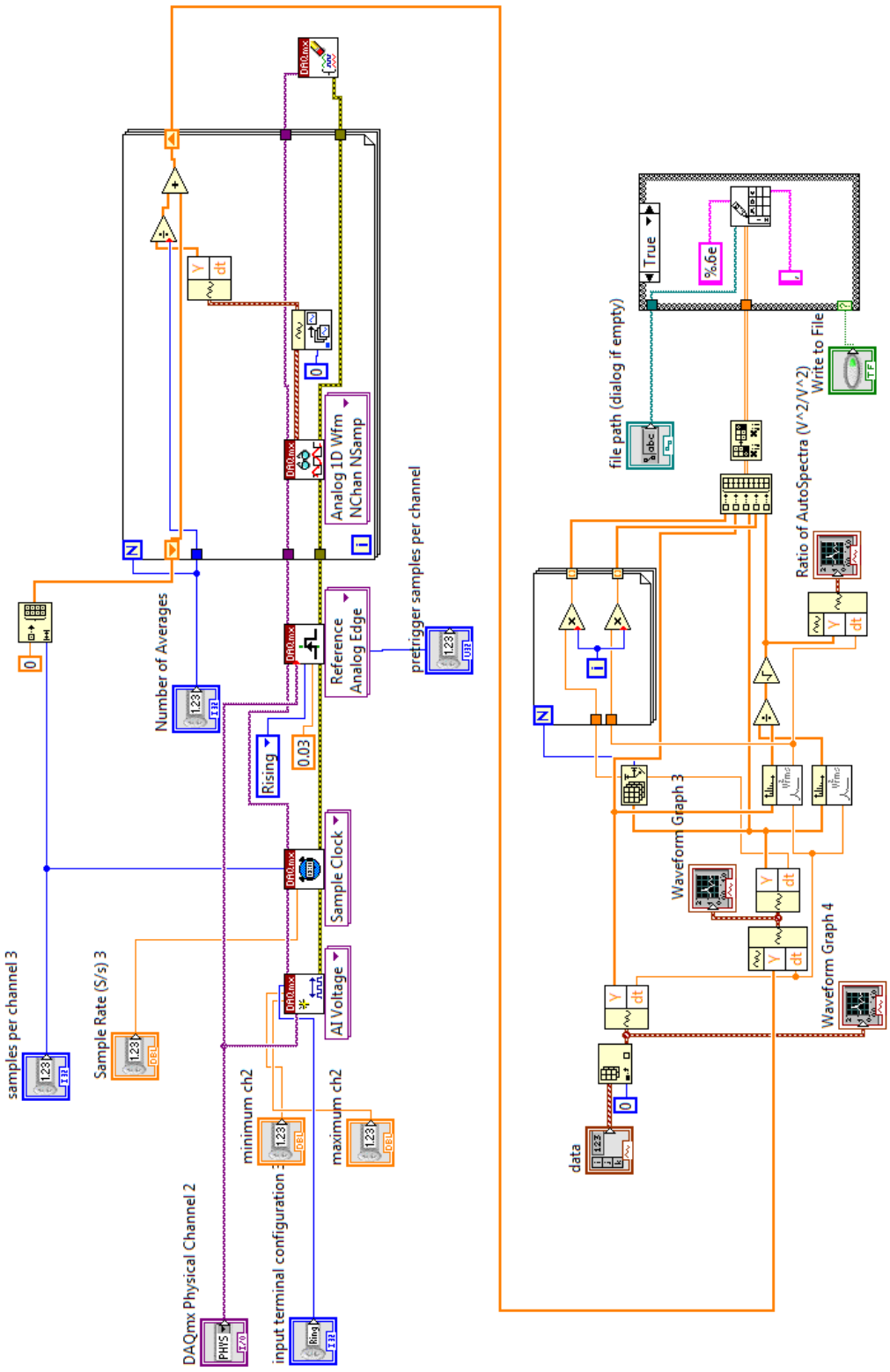

Figure 6-2 - LabVIEW that records LDV measurements

D. Processing of imported data

```
%% Atmospheric Pressure
% 1atm = 29.92inHg = 760 Torr
data = importdata('atmosphere.csv');
time = data(:,1);
Input = data(:,2);   % 10V driving signal with 2 microseconds pulse width (V)
Output = data(:,3)*50;% Response * LDV displacement decoder (nm/V)
InputSquared = Input.^2;
TransFuncOutput = abs(fft(Output))./abs(fft(InputSquared));
N = length(time);                          % Number of data points
T = time(length(time)) - time(1);                 % Duration of signal (sec)
df = 1/T;                                         % frequency increment
TransFuncOutput = TransFuncOutput(1:ceil(N/2));   % Remove data above Nyquist
FreqDomain = (0:length(TransFuncOutput) - 1)*df;

% Remove steady state offset
tfinal = 9e-5;             % The rest of the signal after this point is noise
ssoffset1 = mean(Input(time>tfinal));
ssoffset2 = mean(Output(time>tfinal));
Input = Input-ssoffset1;
Output = Output-ssoffset2;
```

E. Time Domain Method

```
%% Determining the Q factor using time domain method

% Step 1
% Locate the first few peaks
% Process:
% When a peak is found it is added to the peak array, and the boolean
% foundbeak is true. Once it crosses the time axis, foundpeak is false and
% the algorithm looks for the next peak. A desired peak is 'found' when it
% is above the cutoff (determined by inspection) and it is larger than the
% previous 'potential' peak the algorithm found. The time at which the
% peaks are found is recorded as well (used later on).
  cutoff = 0.1;      % First few peaks occur above 0.1nm (Inspection)
  min = 0;
  prevMax = 0;
  foundpeak = false;
  j = 1;
for i=1:size(Output)
   if(Output(i)>cutoff && Output(i)>prevMax)
       peak(j)= Output(i);
       tpeak(j)=time(i);
       prevMax = peak(j);
       foundpeak = true;
   end
   if(Output(i)<min && foundpeak == true)
       j = j+1;
       foundpeak = false;
       prevMax = 0;
   end
end

% Step 2
% Calculating the damping ratio
% 2 'potential' deltas are calcuated and are averaged - the expectation is
% that a better fit will be obtained
PotDelta(1) = log(peak(2)/peak(3));
PotDelta(2) = log(peak(3)/peak(5))/2;
delta = (PotDelta(1)+PotDelta(2))/2;
zeta = delta/sqrt(4*pi^2+delta^2);

% Time difference between peaks (3rd and 4th peak picked randomly)
t1 = tpeak(3);
t2 = tpeak(4);

% The undamped natural frequency
wn = (2*pi)/((t2-t1)*sqrt(1-zeta^2));
wntdomain(6) = wn; % wtdomain keeps track of wn at different pressures

% Plot of the underdamped response of the oscillator
% The reponse intersects the 3rd peak of the signal
% (Response at 3rd peak seems to fit most peaks of output)
datasize = length(time);                    % Length of data set
t = linspace(0,time(datasize),datasize);
A0 = peak(3)/exp(-zeta*wn*tpeak(3));
```

```
ExpDecay = A0*exp(-zeta*wn*t);
figure
plot(t, ExpDecay,'--', time, Output,'-');
hold on
plot(t, -ExpDecay,'--');
xlabel('Time (sec)');
ylabel('Displacement (nm)');
title('cMUT frequency response at 760Torr');
legend('Exponential decay of cMUT response','cMUT response');

% The quality factor is:
Qmeas(6) = 1/(2*zeta);  % Time domain measurement of Q factor
Pmeas(6) = 760;     % atmospheric pressure in Torr
```

F. Frequency Domain Method

```
%% Determining the Q factor using frequency domain
% Assume underdamped natural frequency occurs at 187.5 kHz (or where first
% major peak occurs in transfer function) - This step is done by inspection
 wn = 187.5*10^3*2*pi;
 wnfdomain(7) = wn; % See how wn changes as pressure changes
 margin = 99; % Find index of wn in frequency domain data within 1% of
              % expected value

  for i=1:length(FreqDomain)
     if ((FreqDomain(i)/(wn/(2*pi)))*100 >= margin)
         target = i;
         break
     end
  end

% Find the index and output of frequencies around the target frequency
% (14 points chosen deliberately to be able to generate a nice fit)
for i=1:14
    TFMag(i)= TransFuncOutput(target-6+i);
    TFTargetFreq(i)=FreqDomain(target-6+i);
end

% This next section describes the process that determines the best
% parameters (damping ratio and DC gain) that can best fit the data
% First an initial guess is made for Gdc (DC gain)
% Then, bounds are set for Gdc and z (damping ratio)
% The actual algorithm is described in 'findGdcAndz'
% Note: The initial guess as well as the ranges for Gdc and z are crucial
% for finding the right fit. This step is done iteratively by inspecting
% the map of least squares based on Gdc and z (map is later described in
% funtion) and adjusting the ranges as well as the initial guess
Gdc = 0.002;         % Initial DC gain guess
bounds(1) = Gdc/3;   % Minimum value of DC gain
bounds(2) = Gdc*3;   % Maximum value of DC gain
bounds(3) = 0.02;    % Minimum value of z
bounds(4) = 0.09;    % Maximum value of z

info(:,1) = TFTargetFreq;
info(:,2) = TFMag;
info(1,3) = bounds(1);
info(1,4) = bounds(2);
info(1,5) = bounds(3);
info(1,6) = bounds(4);
info(1,7) = wn;
[Gdc,z] = findGdcAndz(info);

% Plot of measured data around target frequency (wn) and second order system
% based on calculated parameters (Gdc and z). Shin's model is included as
% well
modelData = importdata('modelDataChip7.csv');
f = modelData(:,13);
magO = modelData(:,14);
figure
```

```
H = tf(Gdc*wn^2,[1,2*z*wn,wn^2]);
[mag, phase, freqs] = bode(H);
loglog(TFTargetFreq, TFMag,'ro',freqs/(2*pi), squeeze(mag),'b-',f,magO,'g-');
xlabel('Frequency (Hz)')
ylabel('Magnitude (nm/V^{2})')
title('Transfer function of CMUT at atmospheric pressure (760Torr)')
legend('Measured','Calculated','LEM')

Qcomp(7) = 1/(2*z); % Q factor calculated through Frequency domain
Pcomp(7) = Pmeas(6); % Atmospheric pressure in mbar
```

G. Find DC Gain and Damping Ratio

```
% data is an array
% 1. Array with desired frequencies
% 2. Array with desired magnitudes
% 3. DC Gain minimum value
% 4. DC Gain maximum value
% 4. Damping ratio minimum value
% 5. Damping ratio maximum value
% 6. Undamped natural frequency

function [Gdc,z] = findGdcAndz(data)

Freqs = data(:,1);
DesiredTF = data(:,2);
GdcMin = data(1,3);
GdcMax = data(1,4);
zMin = data(1,5);
zMax = data(1,6);
wn = data(1,7);

% Size of the 2D array
GdcRange = 100;
zRange = 100;

% Number of frequencies
numFreqs = length(Freqs);

% Subvidions
Gdclist=logspace(log10(GdcMin),log10(GdcMax),GdcRange);
zlist=logspace(log10(zMin),log10(zMax),zRange);

% Initialize
min = Inf;
ss = zeros(zRange, GdcRange);

for i=1:zRange
    curz   = zlist(i);
    for j=1:GdcRange

        curGdc = Gdclist(j);
        for k=1:numFreqs
            TransFunc(k)= abs((curGdc*wn^2)/(-
(Freqs(k)*2*pi)^2+2*curz*wn*Freqs(k)*2*pi*sqrt(-1)+wn^2));
            ss(i,j) = ss(i,j)+(DesiredTF(k)-TransFunc(k))^2;
        end
            if(ss(i,j)<min)
                min = ss(i,j);
                Gdc = curGdc;
                z = curz;
            end
    end
end
figure
```

```
[X,Y]=meshgrid(Gdclist,zlist);
pcolor(X,Y,log10(ss))
shading('interp')
colorbar
xlabel('DC gain')
ylabel('Damping Ratio \zeta')
title('Least squares fitting as a function of damping ratio and DC gain')
end
```